Interfacial Properties of Surfactant Monolayers in Microemulsion Systems

by

Daniel Dongyuel Lee

A.B., Harvard University (1990)

Submitted to the Department of Physics
in partial fulfillment of the requirements for the degree of

Doctor of Philosophy in Physics

at the

MASSACHUSETTS INSTITUTE OF TECHNOLOGY

September 1995

Author ....
Department of Physics
August 30, 1995

Certified by...
Sow-Hsin Chen
Professor of Nuclear Engineering
Thesis Supervisor

Certified by...
Mehran Kardar
Professor of Physics
Thesis Co-Supervisor

Accepted by ....
George F. Koster
Chairman, Departmental Committee on Graduate Students

Interfacial Properties of Surfactant Monolayers in Microemulsion Systems

by

Daniel Dongyuel Lee

Submitted to the Department of Physics
on August 30, 1995, in partial fulfillment of the
requirements for the degree of
Doctor of Philosophy in Physics

Abstract

Surfactants in solution can spontaneously self-assemble to form interfacial monolayers which separate mesoscopic regions of water and oil. The statistical mechanics of the surfactant monolayers can explain the rich phase behavior and novel physical properties of microemulsion systems. Here we use x-ray reflectivity to study the intrinsic properties of a single surfactant monolayer at an oil-water interface in equilibrium with a middle-phase microemulsion. We find that the fluctuations of the monolayer are described by large capillary waves due to the small interfacial tension and bending rigidity of the surfactant interface. Next we measure the local geometry of the surfactant monolayers within a bicontinuous microemulsion using isotopic contrast variation and small angle neutron scattering. The mean curvature of the surfactant film is very small and inverts as a function of temperature. We also use neutron reflectivity to relate the surface correlations of the surfactant monolayers near a solid interface to the bulk correlations in the microemulsion. A Ginzburg-Landau theory is employed to interpret our results and to provide further insight into explaining the behavior of the surfactant monolayers in these complex liquids.

Thesis Supervisor: Sow-Hsin Chen
Title: Professor of Nuclear Engineering

Thesis Co-Supervisor: Mehran Kardar
Title: Professor of Physics

Acknowledgments

I could not have written this thesis without the support and friendship of many people. I would like to first thank Sow-Hsin Chen for supervising and guiding my graduate studies and research. His warm personality, enthusiasm for science, and sense of humor made working for him enjoyable, interesting, and amusing. I am also indebted to my co-supervisor, Mehran Kardar, for teaching me statistical mechanics, and to the rest of my thesis committee, David Litster and Richard Yamamoto, for their patience through the rough drafts of this thesis.

I would also like to thank my collaborators Simon Mochrie, Sushil Satija, Chuck Majkrzak, John Barker, Bill Orts, and Dieter Schneider, for letting me use their beam lines and handle their instruments. In 1993, I spent a most pleasurable summer working with Sunil Sinha and Yiping Feng at Exxon. The assistance of countless others at MIT, Brookhaven, and NIST, who barely knew me but stopped to help anyway will never be forgotten.

I have been fortunate to meet and spend time with many friends at MIT. Fellow and former students Bruce Carvalho, Jamie Ku, Yingchun Liu, Brian McClain, Anand Mehta, Larry Saul, David Steel, and Kwong Yee Tan, will always be welcome in my home.

I am also deeply grateful to my parents and my brother, Dean, who have been instrumental in all my accomplishments over the years. Finally, I would like to express my gratitude to my wife, Lisa, for all her love and support. Thank you for providing me with much joy and happiness these past few years.

Contents

4

List of Figures

Chapter 1

Introduction

Since the day when Benjamin Franklin poured oleic acid onto Clapham Pond and observed its calming action upon the surface of the water, scientists have been fascinated with the interfacial properties of surfactants [1]. The cleansing action of liquid soap and its ability to form bubbles and films with intricate shapes and colors can be directly attributed to the unusual molecular composition and statistical mechanics of the surfactant molecules contained within the detergent [2, 3]. Today, these molecules are studied with modern spectroscopic and diffraction techniques, and much progress has been made towards better understanding their chemical and physical properties. Of particular interest is the behavior of surfactants in solution with water and oil and the physics of the self-assembled surfactant interfaces that result. In this introduction, we review a few basic concepts regarding these surfactant films and illustrate some of the extraordinarily rich phase behavior these systems display [4, 5, 6, 7, 8].

1.1 Surfactants in Solution

Figure 1-1 shows the chemical composition of tetraethylene glycol monodecyl ether, otherwise simply abbreviated as $C_{10}E_4$. This molecule is a typical medium-strength, non-ionic surfactant which is composed of two functionally distinct parts. The ten-carbon linear hydrocarbon chain forms an aliphatic "tail" region that prefers non-polar solvents while the ethylene glycol groups form a "head" region that strongly
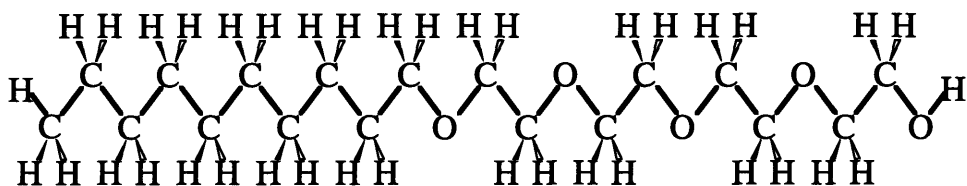
Figure 1-1: Chemical composition of tetraethylene glycol monodecyl ether.

prefers to form hydrogen bonds with water. Thus, when this surfactant is added in solution with water and oil, the amphiphilic molecules spontaneously self-assemble to form two-dimensional interfacial monolayers that segregate distinct water and oil domains rather than disperse into a molecular mixture.

Depending upon various external parameters such as component concentrations, temperature, and pressure, the surfactant monolayers can exist in a wide variety of topologically distinct phases. Some examples of these thermodynamically stable phases are shown in Figure 1-2. The swollen micellar phase consists of oil spheres surrounded by surfactant film in a continuous water medium. In the reverse micellar phase, the roles of water and oil are switched and the surfactant coats water droplets randomly dispersed in oil. Another important example is the lamellar phase which consists of flat surfactant monolayer sheets separating alternating planar stacks of water and oil. In contrast to the geometrical regularity of the lamellar monolayers, the isotropic, bicontinuous microemulsion exhibits a more complex structure containing disordered internal surfactant interfaces. The topological conformation of the water and oil domains in this bicontinuous microemulsion phase resembles the random connectivity of sponges and has led to its characterization as a "plumber's nightmare" [9]. Additional examples of phases not pictured in Figure 1-2 include ordered cubic arrays of spheres, hexagonally-packed arrangements of cylinders, and ordered bicontinuous structures where the surfactant monolayers form minimal surfaces in order to decrease their interfacial areas [10].

These microemulsion systems typically contain water and oil domains with characteristic length scales on the order of hundreds of Ångstroms, although their sizes

9
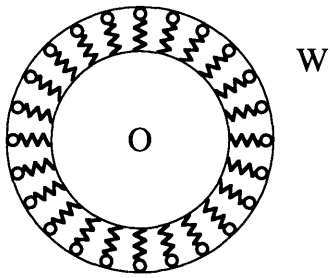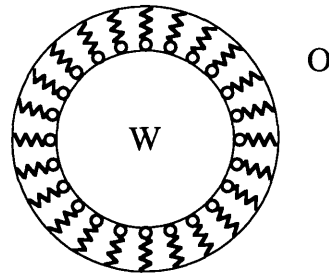
Swollen micelles

Swollen reverse micelles
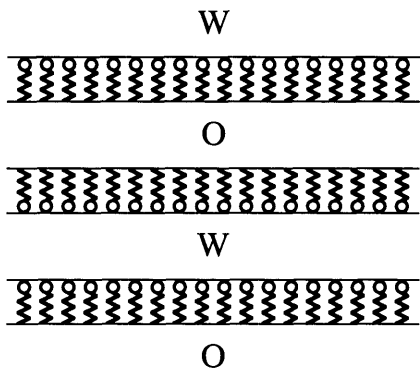
Lamellae
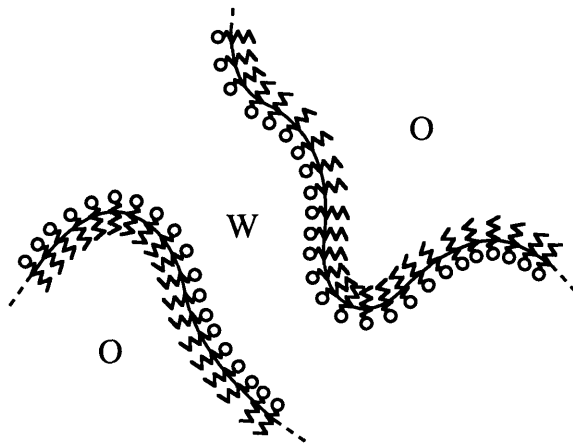
Bicontinuous microemulsion

Figure 1-2: Some representative topologies exhibited by the different phases in surfactant systems.

can easily be varied by tuning the concentrations of the various components. The mesoscopic scale of the structures makes them optically transparent and their unique interfacial and viscoelastic properties are valuable for a wide range of technological applications. In addition to their traditional roles in the detergent, food, cosmetic, and petroleum industries, these surfactant systems have recently found practical applications as pharmaceutical delivery agents and as chemical microreactors for nanofabrication purposes. Along with their industrial significance, the relatively simple sample preparation, rich phase behavior, and intriguing physical characteristics of these complex liquids make them ideally suited for our scientific study.

1.2 Phase Behavior

There are several important factors that determine the phase behavior of microemulsion systems. In solutions containing an ionic surfactant, varying the water salinity can alter the counterion distribution around the surfactants and induce large structural changes in the conformations of the surfactant monolayers [11]. For non-ionic surfactant systems, varying temperature has qualitatively the same analogous effects [12]. Because the structures of non-ionic microemulsions are particularly sensitive to temperature changes, temperature is very valuable as an experimental tuning parameter. At low temperatures, the high-energy hydrophilic interactions between the surfactant head groups and water molecules dominate and the surfactant is more soluble in water than in oil. However, when the temperature is raised, the directional hydrogen bonding between the surfactant and water molecules begin to break apart as thermal fluctuations increase. Entropic effects then drive the surfactant to preferentially solubilize in the oil rather than the water phase.

The effect of temperature can be more clearly seen in the schematic phase diagram pictured in Figure 1-3 [13]. At each temperature, the compositions of the various coexisting phases are represented by individual ternary phase triangles [14, 15]. By following the evolution of the phases as a function of temperature, the resulting triangular prism displaying the overall phase behavior of the surfactant system is

11
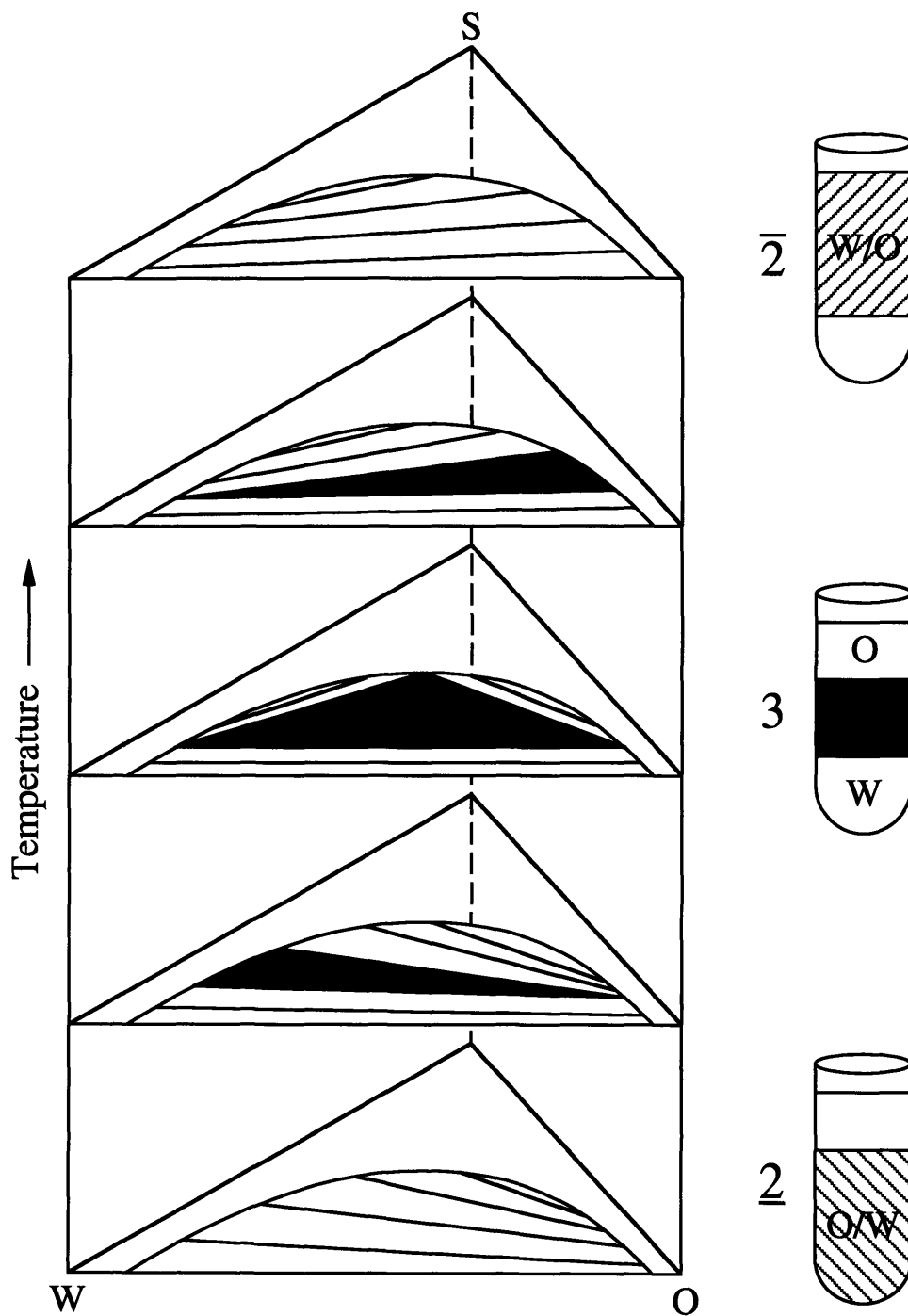
Figure 1-3: Triangular prism showing the phase behavior as a function of temperature and component concentrations.

constructed. At low temperatures, we see predominantly a two phase equilibrium between a lower microemulsion phase and an excess upper oil phase. Because the surfactant preferentially associates with the water phase, the system is unable to emulsify all of the oil. The lower coexisting microemulsion phase contains almost all of the surfactant surrounding small oil droplets within a majority water medium. This conformation allows the system to maximize the favorable water-surfactant interactions [16]. At higher temperatures, the reverse situation occurs with a lower excess water phase in equilibrium with an upper microemulsion phase. In this case, the microemulsion is of the reverse micellar type with water droplets dispersed in an oil medium.

For a small temperature regime between these two extremes, the hydrophilic strength of the surfactant head groups is nearly matched with the hydrophobic nature of the surfactant tails. The temperature at which this hydrophilic-hydrophobic balance occurs is marked by a maximum in the mutual solubility of the surfactant in water and oil. For low surfactant concentrations in this temperature region, a prominent three phase triangular region is observed in the phase diagram [12]. This equilibrium consists of three coexisting phases: a lower water-rich phase, an upper oil-rich phase, and a middle microemulsion phase. Ordered lamellar phases are also commonly observed at higher surfactant concentrations near these temperatures. We have primarily focused our investigation of the interfacial properties of surfactant monolayers under these conditions in the nearly-balanced microemulsion and lamellar phases.

1.3 Bicontinuous Microemulsion

Figure 1-4 is a reproduction of a freeze-fracture electron micrograph taken of a microemulsion at a temperature where the hydrophilicity and hydrophobicity of the surfactant is nearly matched [17]. This picture was taken by rapidly quenching the liquid microemulsion, fracturing the solid sample, coating and shadowing the cleaved surface, and imaging the replica using transmission electron microscopy. This process
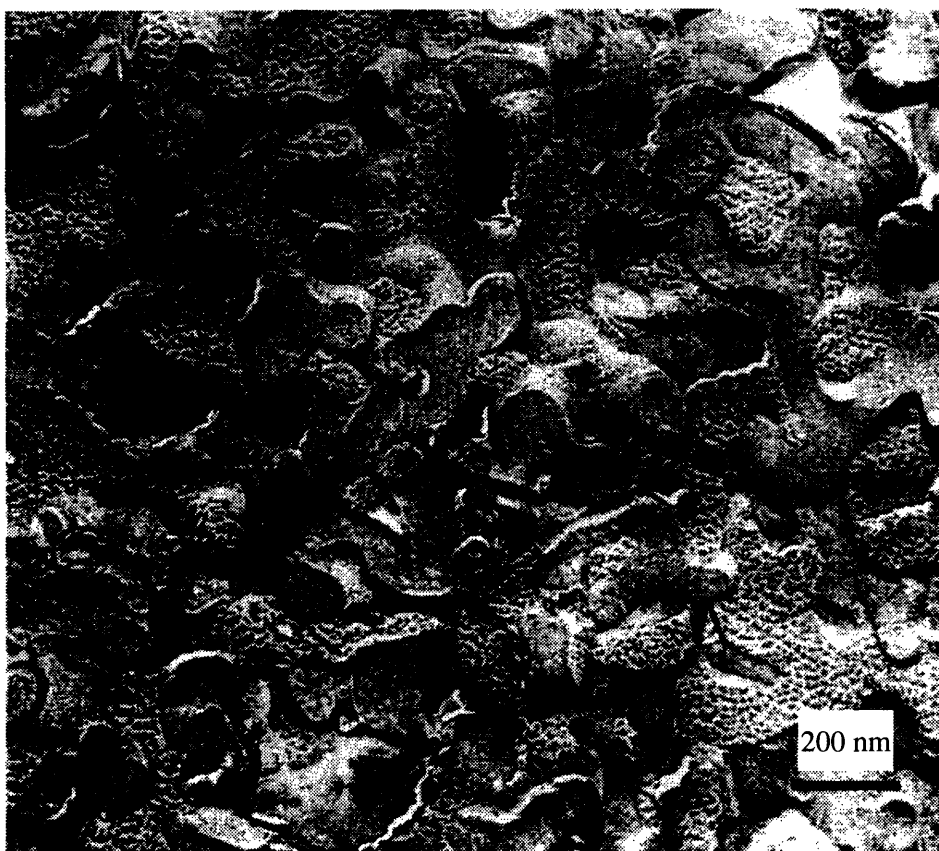
Figure 1-4: Freeze-fracture electron micrograph of a bicontinuous microemulsion.

fortuitously results in an image where the oil regions take on a dimpled texture while the water regions retain a smooth appearance. The surfactant monolayers exist at the interfaces between the water and oil domains but are too thin to be resolved. From this image, we clearly see that the water and oil domains in the microemulsion exhibit a disordered and intricate microstructure that was previously only sketched in Figure 1-2. In contrast to the micellar or well-ordered phases, the geometry of this bicontinuous microemulsion cannot be described in simple geometrical terms. One of our objectives is to formally characterize this phase and the geometry of its surfactant interfaces.

A computer simulation can be used to generate a three-dimensional microstructure for the bicontinuous microemulsion that is consistent with our experimental scattering measurements to be discussed in more detail in Section 4.3 [18, 19, 20, 21]. This simulation allows us to get a better perspective on the disordered spatial conformation of the surfactant monolayers in this phase. First, a Gaussian random field $\Psi(\vec{r})$ is generated by summing together a large number N of cosine waves:

$$\Psi(\vec{r}) = \sqrt{\frac{2}{N}} \sum_{i=1}^{N} \cos(\vec{k_i} \cdot \vec{r} + \varphi_i) \tag{1.1}$$

The phases φ_i and propagation directions $\hat{k}_i$ of the sinusoidal waves are distributed uniformly at random, but the magnitudes of their wave vectors $|\vec{k_i}|$ are chosen from the following spectral distribution function:

$$f(k) = \frac{(b/\pi^2)[a^2 + (b+c)^2]}{(k^2 + c^2)[k^4 + 2(b^2 - a^2)k^2 + (a^2 + b^2)^2]}. \tag{1.2}$$

The parameters a, b, and c are then carefully adjusted in order to fit the experimentally measured small angle scattering data. Once the scalar field $\Psi(\vec{r})$ has been generated in this fashion, the associated surfactant interface is calculated from the locus of the isosurface equation $\Psi(\vec{r}) = 0$. The sixth-order polynomial in Equation 1.2 is necessary in order to keep the surfactant interface from becoming fractal [22]. The parameterization of Equation 1.2 is chosen so that $\pm a \pm bi$ and $\pm ci$ represent

15

the six roots of the polynomial. A representative view of the surfactant monolayer surfaces obtained using this simulation scheme for a microemulsion with parameters $a = 0.023\,\text{Å}^{-1}$, $b = 0.007\,\text{Å}^{-1}$, and $c = 0.05\,\text{Å}^{-1}$ is shown in Figure 1-5.

The water and oil domains seen in Figure 1-5 are each continuously connected in three dimensions so that this microemulsion can truly be called *bicontinuous* [23]. The percolation of both the water and oil domains has been verified experimentally by electrical conductivity and self-diffusion nuclear magnetic resonance measurements [13, 24]. The forms of the bulk and surfactant film scattering predicted by Equation 1.2 also match the observed scattering patterns reasonably well, and taking two-dimensional cross sections of the generated microstructure yields images that resemble the experimental freeze-fracture electron micrograph in Figure 1-4. These results indicate that Figure 1-5 quite accurately represents the actual structure of the bicontinuous microemulsion.

1.4   Phenomenological Description

One aim of scientific inquiry is to explain seemingly complex phenomena in terms of simplifying descriptions. In our situation, the complicated geometrical configuration of the surfactant interfaces in the bicontinuous microemulsion needs to be interpreted within some physical context. One possibility is a microscopic description. This approach attempts to incorporate all the important interactions among the surfactant, water, and oil molecules and then directly calculate the structures of the resulting phases [25, 26, 27]. Although these models have proven useful in elucidating certain aspects of the general phase behavior of these systems, they have yielded only limited insight into the statistical nature of the surfactant film in the bicontinuous phase. Adequately reproducing the long range fluctuations of the surfactant monolayer is quite difficult because the starting point of the microscopic theory is molecular in length. Additionally, the necessary computations for a microscopic theory soon become so complicated that the underlying physics of the system becomes easily obscured.

An approach that is conceptually simple, yet results in a highly detailed descrip-
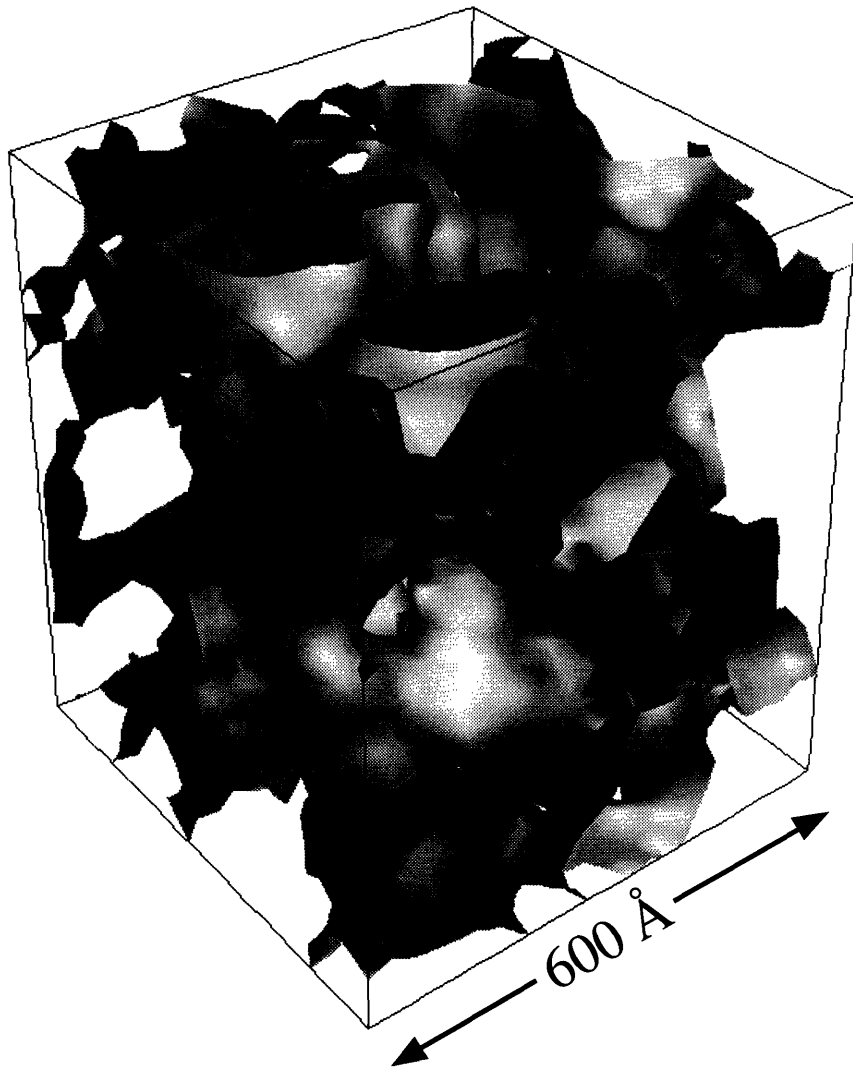
Figure 1-5: Gaussian random wave simulation showing the surfactant interfaces in a bicontinuous microemulsion.
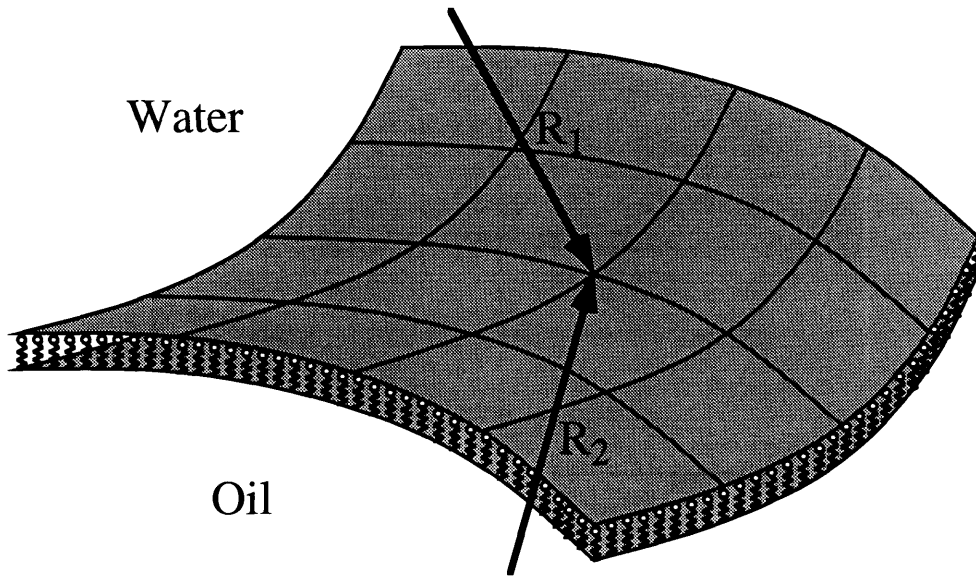
Figure 1-6: Principal radii of curvature at a point on the surfactant monolayer.

tion of the bicontinuous microemulsion phase, considers the surfactant monolayers as idealized surfaces that can be characterized by phenomenological energy considerations [28, 29, 30]. The leading order term in the expansion of the surface free energy is given by the interfacial tension of the monolayer. However, because the surfactant monolayer spontaneously self-assembles to achieve a minimum in this free energy, the effective interfacial tension is very small, and higher-order curvature terms need to be considered. Figure 1-6 depicts a small section of the surfactant film along with the principal radii of curvature R_1 and R_2 at a point on the monolayer. The sign convention is chosen such that curvature concave towards the oil phase is considered positive so that R_1 is negative and R_2 is positive as depicted in Figure 1-6. The mean curvature is defined as the statistical average of the principal curvatures over all points on the interface:

$$C = \frac{1}{2}\left\langle \frac{1}{R_1} + \frac{1}{R_2} \right\rangle.$$
(1.3)

The mean curvature describes the tendency of the surfactant monolayer to curve either towards the oil $(C > 0)$ or towards the water phase $(C < 0)$. On the other

18

hand, the Gaussian curvature is related to the product of the principal curvatures:

$$K = \left\langle \frac{1}{R_1 R_2} \right\rangle. \tag{1.4}$$

The Gaussian curvature is important because it is a topological invariant. According to the Gauss-Bonnet theorem, K is simply related to the number of separate pieces and "handles" in the microemulsion structure [31]. Thus, the Gaussian curvature is positive for spherical microemulsions while it is zero for lamellar phases. In contrast, bicontinuous microemulsions containing many saddle-like surfaces with opposing principal curvatures will exhibit a negative Gaussian curvature.

By expanding the free energy to quadratic order in the principal curvatures of the surfactant monolayer, the following effective interfacial Hamiltonian is obtained [32]:

$$\mathcal{H} = \int \left[\gamma + \kappa \left(\frac{1}{R_1} + \frac{1}{R_2} - 2c_0 \right)^2 + \bar{\kappa} \left(\frac{1}{R_1 R_2} \right) \right] dS \tag{1.5}$$

where γ is the interfacial tension of the monolayer, κ and $\bar{\kappa}$ are phenomenological bending rigidities associated with the mean and Gaussian curvatures respectively, and c_0 is the spontaneous curvature of the surfactant monolayer. In principle, all the relevant physics of the microemulsion is contained within Equation 1.5. Unfortunately, analytically calculating the partition function by summing this Hamiltonian over all possible interfacial configurations of the surfactant monolayers is currently intractable. This difficulty necessitates the use of other theoretical approximations and computer simulations to quantitatively elucidate the statistical mechanics of the surfactant monolayers in the bicontinuous microemulsion. An example is the Gaussian random field model of Equation 1.1 which has been shown to be equivalent to a variational approximation for Equation 1.5 [33].

The phenomenological approach can nonetheless be used to qualitatively describe why under certain conditions, the bicontinuous microemulsion is thermodynamically more stable than the ordered lamellar phase. Assuming a negligible interfacial tension γ, the statistical deviations of a surfactant monolayer away from a flat sheet are controlled by its bending modes as described by Equation 1.5. By calculating how

the surface normals are correlated, the distance over which the interface is essentially flat is derived [28]:

$$\xi_\kappa = a \exp\left(\frac{2\pi\kappa}{kT}\right).$$ (1.6)

This important quantity is known as the persistence length. The molecular length a sets the scale for ξ_κ and is comparable to the size of a surfactant molecule. Because small fluctuations have no effect on the topology of the monolayer and thus contribute little to the Gaussian curvature K, the persistence length depends only upon the bending rigidity κ and not on $\bar{\kappa}$. The exponential dependence in Equation 1.6 implies that when the κ is large, the surfactant monolayers are flat over macroscopic distances and the lamellar phase is preferred. However, if κ is comparable to thermal energies, entropic considerations become more important than the energy cost associated with bending the surfactant interfaces. Under these conditions, the random bicontinuous microemulsion becomes more stable than the lamellar phase. Thus, the phenomenological description of Equation 1.5 is very useful for a basic understanding of the interfacial properties of surfactant monolayers and the phase behavior of microemulsion systems.

Chapter 2

Small Angle Scattering and Reflectivity

Imaging microemulsions using standard optical techniques is not possible because of the mesoscopic sizes of the water and oil domains in these systems. By far the most detailed information about the structure and dynamics of the surfactant monolayers within microemulsions has come from x-ray and neutron scattering studies. However, because the relevant length scales describing the monolayers are hundreds of times larger than the typical wavelengths of the probes, the most interesting part of the scattering pattern lies in the region at very small angles from the incident beam. In this chapter, we present some basic formalism for describing the scattering from interfaces and illustrate what can be learned by analyzing the scattering patterns in the small angle regime [34].

2.1   Born Approximation

X-rays and neutrons interact very weakly with most matter. The physics of their atomic and nuclear interactions are well understood and their strong penetrating power allows them to effectively probe liquid systems. Figure 2-1 schematically illustrates a typical scattering experiment. A beam of x-rays or neutrons is monochromated, collimated, and directed into the sample with a well-defined wavelength λ
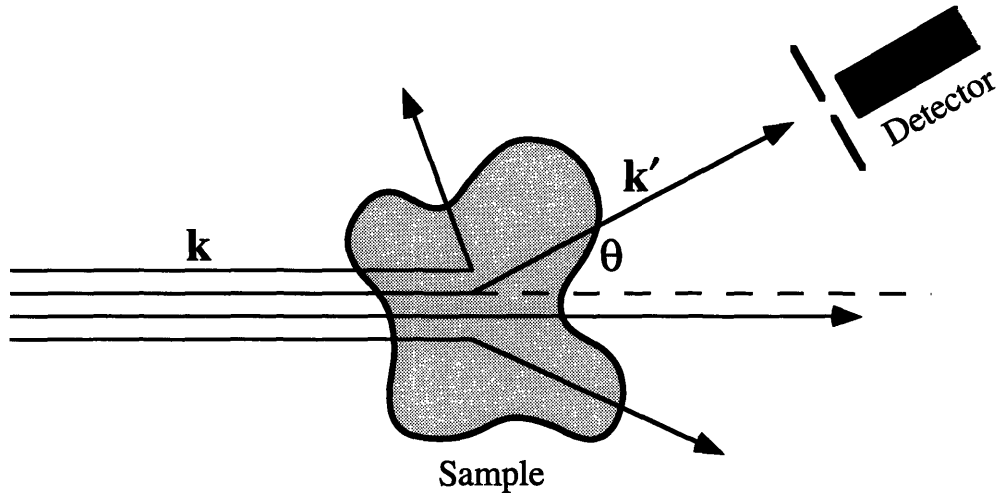
Figure 2-1: Typical configuration for a scattering experiment.

and incident wave vector $\vec{k}$. The resulting scattering pattern is then measured using detectors at various scattering angles θ. Changes in the kinetic energy of the probe upon passing through the sample can also be determined to deduce information about time-dependent dynamical fluctuations, but for our purposes we will focus on *elastic* scattering events associated with no energy change. The scattered wave vector $\vec{k}'$ then has the same magnitude as the incident wave vector $\vec{k}$:

$$k = \left|\vec{k}\right| = \left|\vec{k}'\right| = \frac{2\pi}{\lambda}, \tag{2.1}$$

and the magnitude of the momentum transfer $\vec{Q} = \vec{k}' - \vec{k}$ depends only upon the scattering angle:

$$\left|\vec{Q}\right| = 2k\sin\frac{\theta}{2}. \tag{2.2}$$

The differential cross section is defined to be the intensity of scattered particles per unit solid angle divided by the incident flux. Angular variations in the scattered beam intensity measured by the detector arise from constructive and destructive interference of scattered spherical waves from atoms in the sample. Consider an atom located at a position $\vec{R}_i$ relative to an origin in the sample. It has a characteristic scattering length b_i, which for x-rays is directly proportional to its atomic number,
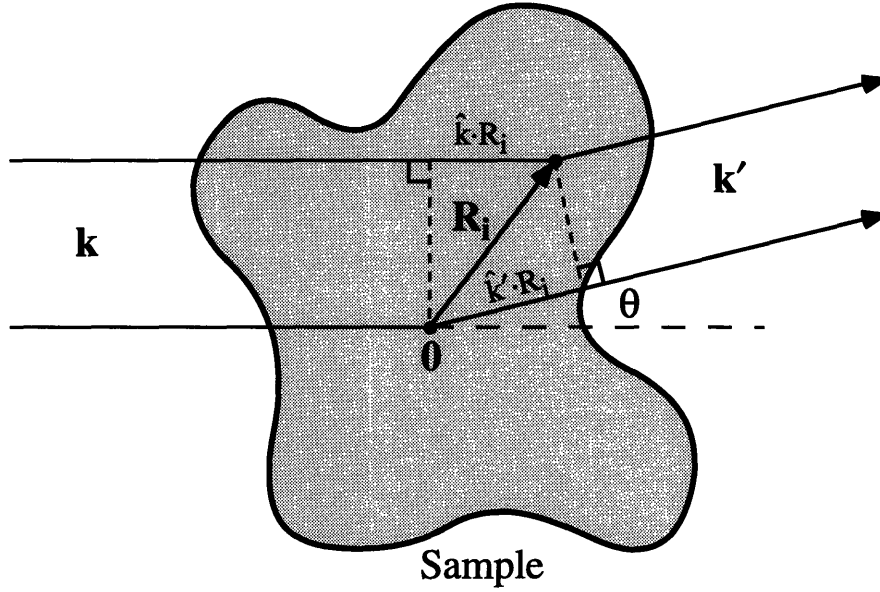
Figure 2-2: Difference in path lengths from scattering in the sample.

and for neutrons is related to its nuclear isotope and spin. As shown in Figure 2-2, the path difference between scattering from the atom at $\vec{R}_i$ and from the origin is given by the expression $(\hat{k} \cdot \vec{R}_i - \hat{k}' \cdot \vec{R}_i)$. The total amplitude of the scattered beam is calculated by summing up the relative phase contributions from all the atoms in the sample. The differential cross section is then given by taking the square of the magnitude of the scattering amplitude:

$$\frac{d\sigma}{d\Omega}(\theta) = \left| \sum_i b_i \exp\left[ik(\hat{k} - \hat{k}') \cdot \vec{R}_i\right] \right|^2 \tag{2.3}$$

$$= \left| \int \rho(\vec{r}) e^{-i\vec{Q}\cdot\vec{r}} d\vec{r} \right|^2. \tag{2.4}$$

The scattering length density $\rho(\vec{r})$ is defined by statistically averaging the positions of the atoms in the sample:

$$\rho(\vec{r}) = \left\langle \sum_i b_i \delta(\vec{r} - \vec{R}_i) \right\rangle. \tag{2.5}$$

Equation 2.4 states that the scattering intensity is related to the square of the

23

Fourier transform of the scattering length density. This important result can also be derived starting with the time-independent Schrödinger equation for neutrons [35]:

$$\frac{\hbar^2}{2m}(\vec{\nabla}^2 + k^2)\psi(\vec{r}) = U(\vec{r})\psi(\vec{r}) \tag{2.6}$$

where m is the mass of the neutron, $\psi(\vec{r})$ is its wave function, and the potential function is related to the scattering length density $U(\vec{r}) = (2\pi\hbar^2/m)\rho(\vec{r})$.

In order to obtain the scattering distribution from Equation 2.6, we first consider the related differential equation:

$$(\vec{\nabla}_r^2 + k^2)G(\vec{r}, \vec{r}') = -4\pi\delta(\vec{r} - \vec{r}'). \tag{2.7}$$

Its solution is the Green's function:

$$G(\vec{r}, \vec{r}') = \frac{e^{ik|\vec{r}-\vec{r}'|}}{|\vec{r} - \vec{r}'|}. \tag{2.8}$$

Equation 2.6 can be converted into an integral equation by summing over the potential source terms using $G(\vec{r}, \vec{r}')$. The wave function can then be expressed as:

$$\psi(\vec{r}) = e^{i\vec{k}\cdot\vec{r}} - \int \frac{e^{ik|\vec{r}-\vec{r}'|}}{|\vec{r} - \vec{r}'|}\rho(\vec{r}')\psi(\vec{r}')\,d\vec{r}'. \tag{2.9}$$

The first Born approximation involves replacing the complete wave function $\psi(\vec{r}')$ in the integral of Equation 2.9 with the incident wave $e^{i\vec{k}\cdot\vec{r}}$. For large distances away from the interaction region ($r \to \infty$), this substitution yields the expression:

$$\psi(\vec{r}) \approx e^{i\vec{k}\cdot\vec{r}} - \frac{e^{ikr}}{r}\int e^{-i(k\hat{r}-\vec{k})\cdot\vec{r}'}\rho(\vec{r}')\,d\vec{r}'. \tag{2.10}$$

From the amplitude of the spherical wave in the second term of Equation 2.10, we see that the scattering amplitude is equivalent to the Fourier transform of the scattering length density. Thus, this simple quantum mechanical description also results in the differential scattering cross section given in Equation 2.4.
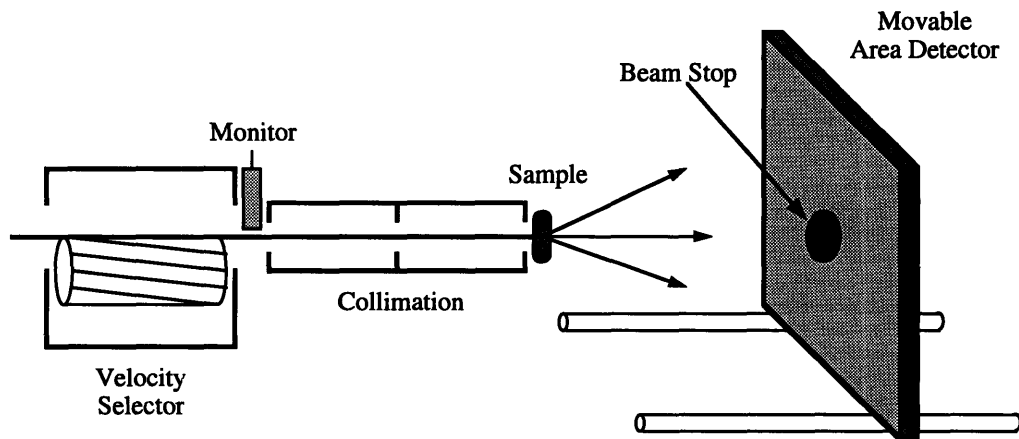
Figure 2-3: Schematic diagram of a small angle neutron scattering instrument.

2.2 Small Angle Scattering

According to Equation 2.4, relatively large inhomogeneities in the sample result in scattering variations at small momentum transfers [36]. Sophisticated instrumentation and specialized techniques have been developed to efficiently collect and analyze this small angle scattering. Figure 2-3 is a schematic diagram illustrating a typical small angle neutron scattering (SANS) instrument. Neutrons from the cold source of a nuclear reactor are monochromated using a mechanical velocity selector and the resulting flux is monitored with a detector. The neutron beam is then collimated with a set of pinholes and directed into a thin sample. The resulting scattering is measured with an area detector which is moved along a set of tracks to capture various ranges of scattering angles and neutron wave vector transfers. A beam stop is normally used to protect the detector from the high intensity of the incident beam. It can be moved out of position after attenuating the neutron beam in order to determine the unscattered fraction of neutrons transmitted through the sample compared to an empty scattering cell.

Figure 2-4 displays a scattering pattern that was measured for a sample consisting of 20% $C_{10}E_4$, 40% D_2O, and 40% octane at $T = 22\,°C$. This data was taken on the 30 m NSF SANS instrument at the National Institute of Standards and Technology at
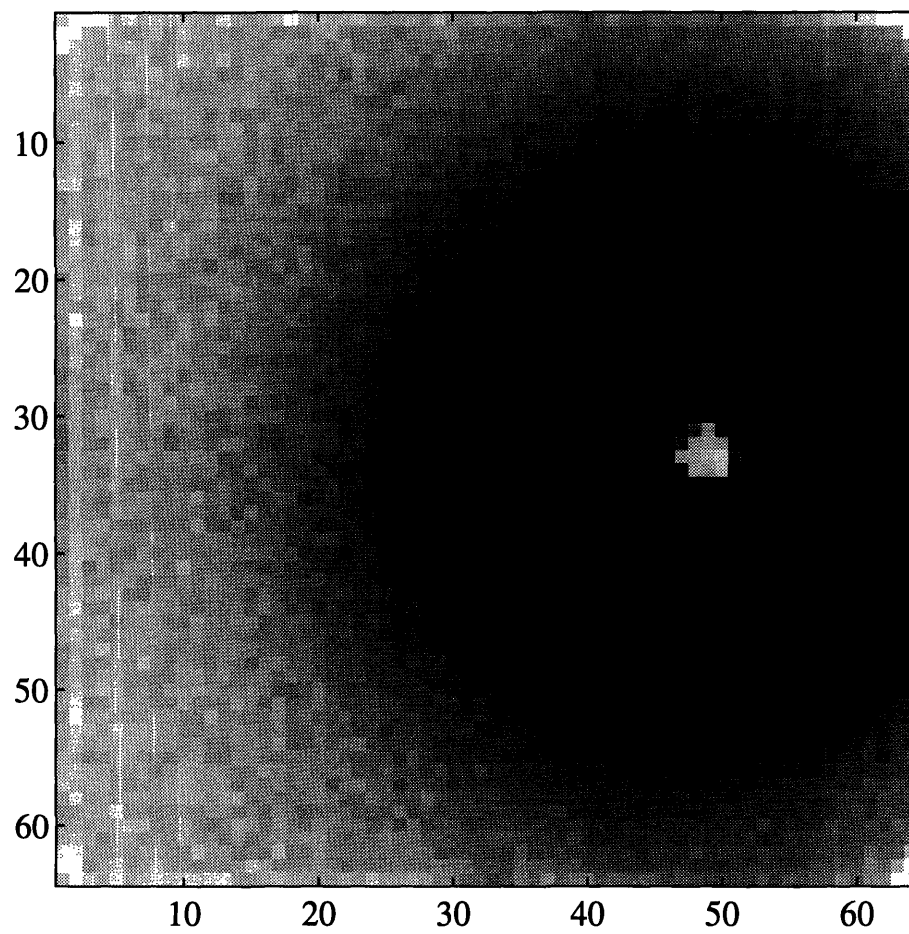
Figure 2-4: Two-dimensional SANS pattern from a lamellar sample.

a neutron wavelength of $\lambda = 5.0\,\text{Å}$ using a $64 \times 64\ \text{cm}^2$ area detector at a distance of 4.00 meters. The center of the neutron beam has been offset horizontally in order to measure a larger range of scattering angles. This particular sample is in the lamellar phase and the prominent ring of scattered neutrons at an angle $\theta \approx 1.8°$ is due to Bragg reflections from the lamellar planes in the sample.

Before we can quantitatively analyze this scattering pattern, the data must be corrected by measuring and subtracting the background radiation and scattering from the quartz sample holder. The efficiency of the detector also needs to determined using the incoherent scattering of H_2O. The unreliable data near the edges of the area detector and around the beam stop are masked out and the pixels are circularly averaged to give the scattering as a one-dimensional function of the neutron momentum transfer Q. In order to normalize the scattering intensity, standards with known cross-sections are measured and the appropriate calibration factor for the instrument is determined [37]. Using this normalization constant and the measured transmission of the sample, the differential scattering cross section can be reduced to an absolute scale. We have developed computational routines that allow us to easily and rapidly implement this background subtraction and normalization for large numbers of experimental data sets. For the data shown in Figure 2-4, this reduction procedure results in the scattering curve plotted in Figure 2-5.

The most prominent feature of Figure 2-5 is the sharp peak at $Q_{\max} \simeq 0.04\,\text{Å}^{-1}$ that corresponds to the dark scattering ring in Figure 2-4. The position of this peak implies a lamellar repeat distance of $D = 2\pi/Q_{\max} \simeq 160\,\text{Å}$, and the limited resolution of the instrument accounts for the width of the scattering peak. We also see a relatively slow decay in the scattering at larger Q values. Incoherent scattering from the hydrogen nuclei in the sample contributes a flat background to the measured pattern. Subtracting this background level leads to a decay at large angles that is roughly proportional to Q^{-4}. In order to explain the origin of this scattering, consider the formula for the differential cross-section derived above in Section 2.1:

$$S(\vec{Q}) = \frac{1}{V}\frac{d\sigma}{d\Omega}(\vec{Q}) = \frac{1}{V}\left|\int \rho(\vec{r})e^{-i\vec{Q}\cdot\vec{r}}\,d\vec{r}\right|^2 \tag{2.11}$$
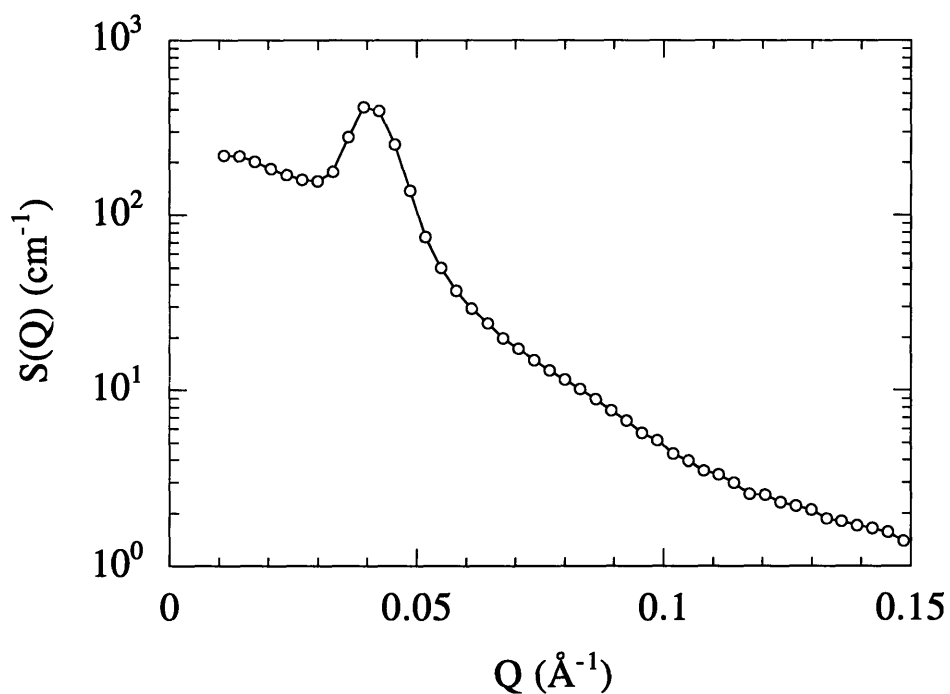
Figure 2-5: Reduced scattering curve for a lamellar sample.

By expanding Equation 2.11, we get:

$$S(\vec{Q}) = \frac{1}{V} \left[\int \rho(\vec{r}) e^{-i\vec{Q}\cdot\vec{r}} d\vec{r} \cdot \int \rho(\vec{r'}) e^{i\vec{Q}\cdot\vec{r'}} d\vec{r'} \right] \tag{2.12}$$

$$= \frac{1}{V} \int \rho(\vec{r})\rho(\vec{r'}) \, e^{i\vec{Q}\cdot(\vec{r'}-\vec{r})} \, d\vec{r} d\vec{r'} \tag{2.13}$$

$$= \int \Gamma(\vec{r'} - \vec{r}) \, e^{i\vec{Q}\cdot(\vec{r'}-\vec{r})} \, d(\vec{r'} - \vec{r}) \tag{2.14}$$

where we can define the correlation function [38]:

$$\Gamma(\vec{x}) = \langle \rho(0)\rho(\vec{x}) \rangle - \langle \rho(0) \rangle^2 . \tag{2.15}$$

The square of the mean scattering length density has been subtracted so that in disordered phases at large distances, $\Gamma(\vec{x})$ goes to zero. For isotropic samples, the correlation function does not contain any angular dependence and depends only upon

distance so that Equation 2.14 can be written as:

$$S(Q) = \int_0^\infty \Gamma(R) \frac{\sin QR}{QR} \cdot 4\pi R^2 dR. \tag{2.16}$$

Integrating Equation 2.16 by parts leads to a large Q expansion of the scattering intensity:

$$S(Q) = -\frac{8\pi\Gamma'(0)}{Q^4} + \frac{16\pi\Gamma'''(0)}{Q^6} - O(Q^{-8}). \tag{2.17}$$

From this equation, we see that the scattering intensity at large angles is explicitly related to the behavior of the correlation function at short length scales.

Now suppose that the scattering volume consists of two separate but dispersed phases with volume fractions ϕ_1 and ϕ_2, and scattering length densities ρ_1 and ρ_2. The value of the correlation function at R is related to the probability that two random points in the medium separated by distance R are either in the same phase or different phases. For $R = 0$, we see that the points will always be inside the same phase. When R is very small, the probability that the two points are in different phases is proportional to how much interfacial area per volume A/V there is separating the two phases. In particular, the short range behavior of the correlation function is given by:

$$\Gamma(R) \approx (\rho_1 - \rho_2)^2 \left[\phi_1\phi_2 - \frac{A}{4V}R + O(R^2) \right]. \tag{2.18}$$

Therefore, from Equation 2.17, the decay in scattering intensity is directly proportional to the interfacial area per volume between the two phases and inversely proportional to the fourth power of the wave vector transfer [39]:

$$S(Q) \approx 2\pi(\rho_1 - \rho_2)^2 \left(\frac{A}{V}\right) \frac{1}{Q^4}. \tag{2.19}$$

Equation 2.19 is known as Porod's law and indicates that by fitting the scattering at relatively large angles, the interfacial area per volume of a two-phase medium can be measured. We will use this result later to determine the curvatures of the surfactant monolayers in a bicontinuous microemulsion.
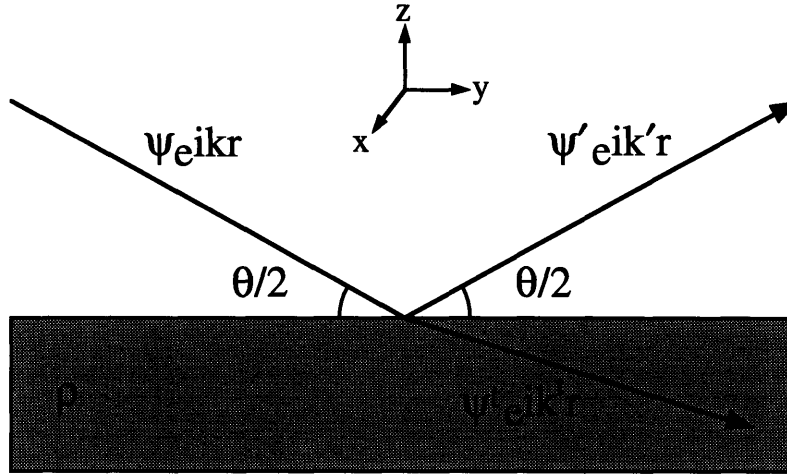
Figure 2-6: Geometry for reflection from a single flat surface.

2.3 Reflectivity

In many circumstances, the interfacial structure of samples near flat surfaces is of particular interest. In these cases, it is more convenient to measure the radiation reflected off the surface rather than the scattering transmitted through the sample. Figure 2-6 shows the geometry for reflection at the interface of a uniform medium with scattering length density ρ. The incident, reflected, and transmitted wave vectors are respectively denoted $\vec{k}$, $\vec{k}'$, and $\vec{k}^t$. The amplitudes of the various wave functions are similarly given by ψ, ψ', and ψ^t.

Due to the higher potential induced by the scattering length density of the reflecting medium, the magnitudes of the incident, reflected, and transmitted momenta are related according to:

$$\left|\vec{k}\right|^2 = \left|\vec{k}'\right|^2 = \left|\vec{k}^t\right|^2 + 4\pi\rho. \tag{2.20}$$

Continuity of the wave functions above and below the interface demands that the wave vector components parallel to the interface are equal:

$$k_x = k_x' = k_x^t \tag{2.21}$$

$$k_y = k_y' = k_y^t \tag{2.22}$$

while the components perpendicular to the interface are given by:

$$k'_z = -k_z \tag{2.23}$$

$$k^t_z = \sqrt{k^2_z - 4\pi\rho}. \tag{2.24}$$

Matching the values of the wave functions and their first derivatives above and below the interface implies:

$$\psi + \psi' = \psi^t \tag{2.25}$$

$$k_z(\psi - \psi') = k^t_z\psi^t. \tag{2.26}$$

Solving these equations for the ratio of the reflection to the incident amplitudes results in the expression:

$$r_F(Q) = \frac{\psi'}{\psi} = \frac{k_z - k^t_z}{k_z + k^t_z}. \tag{2.27}$$

The intensity of the reflected beam normalized by the incident beam intensity can then be written in terms of the wave vector transfers $Q = 2k_z$ and $Q^t = 2k^t = \sqrt{Q^2 - 16\pi\rho}$:

$$R_F(Q) = |r_F(Q)|^2 = \left|\frac{Q - Q^t}{Q + Q^t}\right|^2. \tag{2.28}$$

Known as Fresnel's law, Equation 2.28 gives the dependence of the reflected intensity as a function of the scattering angle.

At small angles, Q^t is purely imaginary so that the reflectivity R_F is equal to unity. This condition is known as total external reflection and indicates that because the transmitted wave is evanescent and non-propagating, all of the incident radiation is reflected off the interface. Note that at large angles, Equation 2.28 decays according to the form:

$$R_F(Q) \approx \frac{16\pi^2\rho^2}{Q^4}. \tag{2.29}$$

Aside from some geometrical factors, Equation 2.29 is equivalent to Porod's law for small angle scattering given in Equation 2.19.

Reflectivity can also be used to probe an arbitrary interfacial structure whose
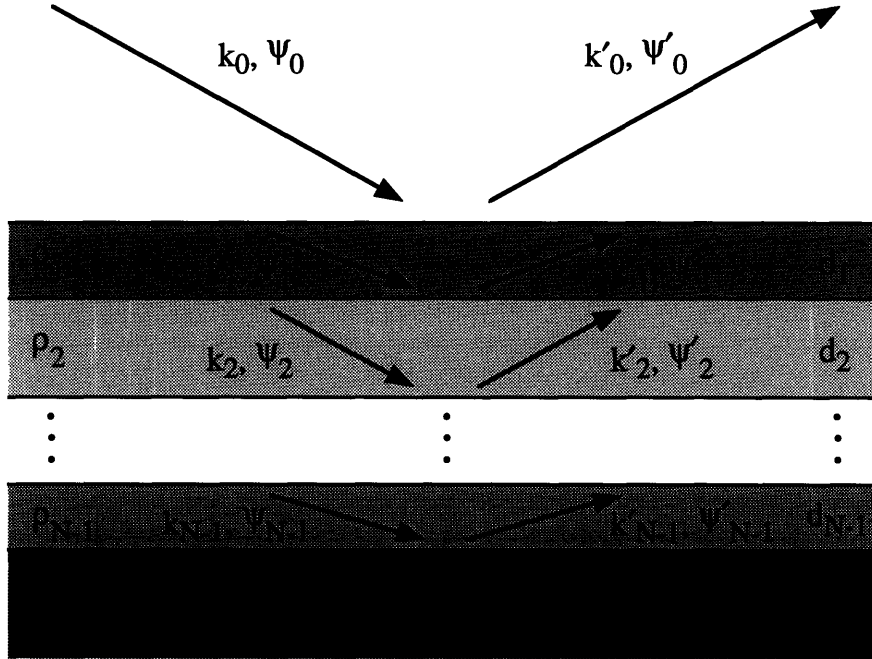
Figure 2-7: Reflection from a structure with N layers.

scattering length density varies as a function of depth. As shown in Figure 2-7, we model the interface as consisting of N layers, each described by a thickness d_i and scattering length density ρ_i. The parallel components of the wave vectors in the ith layer are equal to the parallel components of the incident wave vector $\vec{k}_0$:

$$k_{i,x} = k'_{i,x} = k_{0,x} \tag{2.30}$$

$$k_{i,y} = k'_{i,y} = k_{0,y}. \tag{2.31}$$

The perpendicular components are given by:

$$k_{i,z} = -k'_{i,z} = \sqrt{k_{0,z}^2 - 4\pi\rho_i}. \tag{2.32}$$

At the interface between the ith and $(i+1)$th layers, continuity of the wave functions and their first derivatives require that the amplitudes of the wave functions in the

32

layers are related according to [40]:

$$r_i = \frac{r_{i+1} + r_F^i}{1 + r_{i+1}r_F^i} \tag{2.33}$$

where we define the reflectance $r_i = \psi_i'/\psi_i$ and the Fresnel coefficient:

$$r_F^i = \frac{k_{i,z} - k_{i+1,z}}{k_{i,z} + k_{i+1,z}}. \tag{2.34}$$

Equation 2.33, known as the Parratt formula, describes a recursive relationship between the reflectance of any layer in terms of reflectance in the layer below. Thus, in order to obtain the reflectivity $|\psi_0'/\psi_0|^2$ from the top surface, we first start at the bottom interface and calculate the reflectance $r_{N-1} = r_F^{N-1}$ using Fresnel's law. We then continue upward through the $(N-1)$th layer with thickness d_{N-1} and phase shift the reflectance by the factor $\exp(2ik_{N-1,z}d_{N-1})$. Using the Parratt formula in Equation 2.33, the reflectance coefficient r_{N-2} is determined. This coefficient is then phase shifted and used to calculate r_{N-3}. This process is continued until the top interface is reached. Thus, given the thicknesses and scattering length densities of an arbitrary multilayered system, this procedure can be used to determine the reflectivity at any wave vector transfer $Q = 2k_0$.

In an actual experiment, the reflectivity is measured at various angles from which the scattering length density profile of the sample needs to be deduced. Unfortunately, since only the magnitude of ψ_0'/ψ_0 is measured and not its phase, the determination of the scattering length densities is not unique. Additional information about the sample must be used to constrain the model parameters and fit the measured reflectivity data using Equation 2.33. In practice, this procedure works resonably well and the calculated scattering length density profile is generally quite accurate. This type of ambiguity often arises in inverse scattering problems, and for small angle scattering measurements, the lack of phase information in the scattering pattern $S(\vec{Q})$ implies that only the correlation function $\Gamma(\vec{r})$ and not the scattering length density $\rho(\vec{r})$ can be uniquely determined.
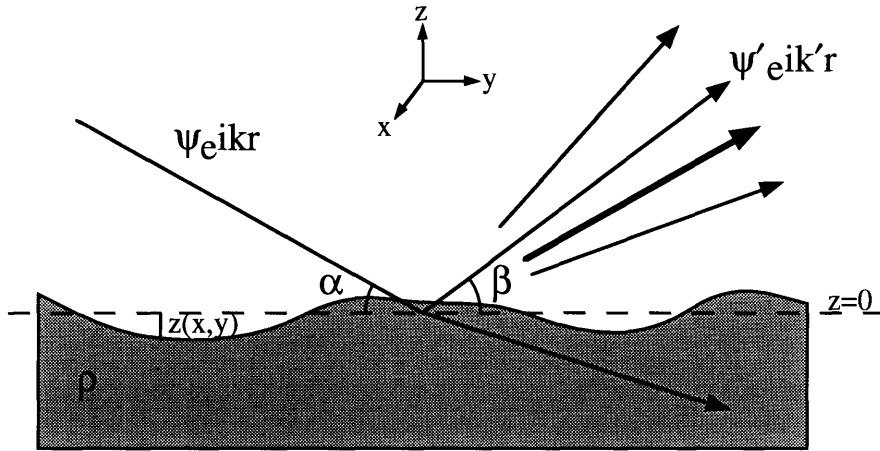
Figure 2-8: Diffuse scattering arising from a rough interface.

2.4 Rough Interfaces

In the previous section, reflection from perfectly flat interfaces was described. Here we consider the reflectivity and diffuse scattering arising from a rough interface. Figure 2-8 depicts a rough surface which is described in terms of its deviations away from the average flat surface $z(x, y) = 0$. We assume that the function $z(x, y)$ is relatively small and single-valued so that the interface is not too rough and does not contain any overhangs. The incoming beam makes an incident angle α with the surface and the scattered wave is measured at angle β. If the interface were perfectly smooth, the only scattered radiation would be the specular reflected beam at $\beta = \alpha$. A rough interface, on the other hand, gives rise to diffuse scattering at all angles β in addition to the specular reflection.

The scattering from the interface can be described in terms of the Born approximation. In this case, Equation 2.4 is first converted to a surface integral over the $z = 0$ plane using Gauss's theorem:

$$S(\vec{Q}) = \frac{1}{V} \left| \frac{i\rho}{Q_z} \int dx \, dy \, e^{-i[Q_x x + Q_y y + Q_z z(x,y)]} \right|^2 . \tag{2.35}$$

Expanding the square yields the more useful expression:

$$S(\vec{Q}) = \frac{\rho^2}{VQ_z^2} \int dx\,dy\,dx'\,dy'\,e^{-i[Q_x(x-x')+Q_y(y-y')]}e^{-iQ_z[z(x,y)-z(x',y')]} \qquad (2.36)$$

$$= \frac{\rho^2}{Q_z^2}\frac{A}{V} \int dx\,dy\,e^{-i[Q_x x + Q_y y]}e^{-Q_z^2[z(x,y)-z(0,0)]^2/2} \qquad (2.37)$$

$$= \rho^2 \left(\frac{A}{V}\right)\frac{e^{-\sigma^2 Q_z^2}}{Q_z^2} \int dx\,dy\,e^{-i[Q_x x + Q_y y]}e^{Q_z^2\langle z(x,y)\,z(0,0)\rangle} \qquad (2.38)$$

where A is the area of the interface and $\sigma^2 = \langle z(0,0)^2\rangle$ is the mean square roughness of the interface. Equation 2.38 can be decomposed into a specular and diffuse component. The scattering concentrated at the specular condition $\alpha = \beta$ is given by:

$$S(\vec{Q}) = \rho^2 \left(\frac{A}{V}\right)\frac{e^{-\sigma^2 Q_z^2}}{Q_z^2}\,\delta(Q_x)\delta(Q_y). \qquad (2.39)$$

Expressed in terms of the ratio of reflected to incident beam intensities, the specular reflectivity is written:

$$R(Q) = \frac{16\pi^2\rho^2}{Q^4}e^{-\sigma^2 Q^2} \simeq R_F(Q)e^{-\sigma^2 Q^2} \qquad (2.40)$$

Thus, the main effect of roughness is to attenuate the magnitude of the reflectivity at large angles with a Debye-Waller factor.

In most measurements of the diffuse scattering component of Equation 2.38, the instrumental resolution is usually very wide in the transverse x direction, effectively integrating over the wave vector components Q_x. The diffuse scattering within the Born approximation can then be written:

$$S(Q_y, Q_z) = \rho^2 \left(\frac{A}{V}\right)\frac{e^{-\sigma^2 Q_z^2}}{Q_z^2} \int dy\,e^{-iQ_y y}\left[\exp\left(Q_z^2\langle[z(0)\,z(y)\rangle\right) - 1\right]. \qquad (2.41)$$

A more complete treatment using a distorted wave Born approximation results in the slightly more complicated expression [41, 42]:

$$S(Q_y, Q_z) = \rho^2 |t_\alpha|^2 |t_\beta|^2 \left(\frac{A}{V}\right)\frac{e^{-\sigma^2\left[\text{Re}(Q_z^t)^2 - \text{Im}(Q_z^t)^2\right]}}{|Q_z^t|^2}$$

35

$$\times \int dy\, e^{-iQ_y y} \left[\exp\left(\left|Q_z^t\right|^2 \langle z(0)\, z(y)\rangle\right) - 1\right] \qquad (2.42)$$

where $t_\alpha = 1 - r_F(\alpha)$ and $t_\beta = 1 - r_F(\beta)$ are the Fresnel transmission coefficients for a flat interface at incident angles α and β. Equation 2.42 states that the diffuse scattering of the interface is related to the Fourier transform of its correlation function $\langle z(0)\, z(y)\rangle$. Thus, the scattering from a rough interface depends upon the correlations in height along its surface. We will use this result in the next chapter to study the properties of a saturated surfactant monolayer.

Chapter 3

X-ray Reflectivity from a Surfactant Monolayer in Equilibrium with a Middle-Phase Microemulsion

In order to study some of the intrinsic properties of surfactant monolayers, we decided to isolate and measure a *single* oil-water interface saturated with surfactant that is in equilibrium with a bicontinuous microemulsion. This chapter includes a description of the experimental procedure we used to prepare and measure this system and an analysis of the resulting reflectivity and diffuse scattering arising from the surfactant monolayer [43].

3.1   Experimental Setup

Figure 3-1 displays the ternary phase diagram for the triethylene glycol monooctyl ether (C_8E_3), water, and decane system at T = 22 °C, the temperature at which the surfactant is most mutually soluble in the water and oil. As discussed above in Section 1.2, the phase diagram at low surfactant concentrations exhibits a prominent three-phase equilibrium. When a solution is prepared with concentrations inside this
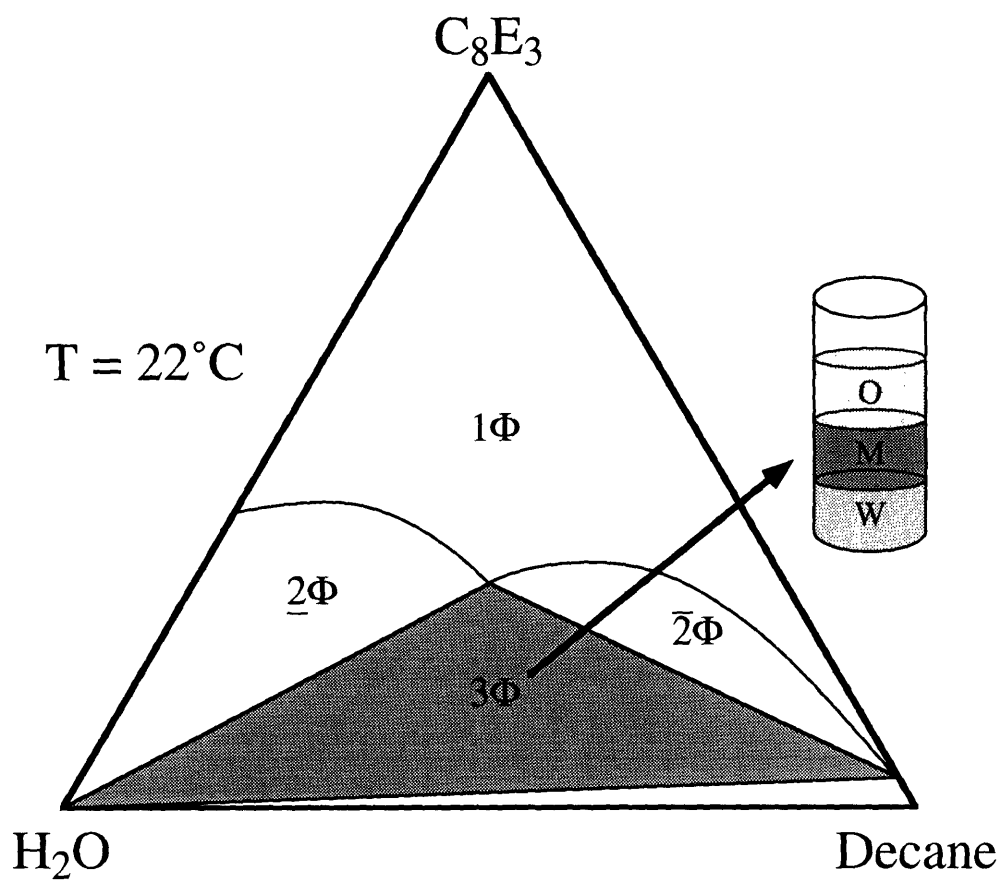
Figure 3-1: Ternary phase diagram for the C_8E_3-water-decane system at $T = 22\,°C$.

triangular three-phase region, a surfactant-rich bicontinuous microemulsion forms in coexistence with an oil-rich upper phase and a water-rich lower phase. The middle-phase microemulsion is quite remarkable in that it does not wet the other two phases. Therefore, when most of the microemulsion phase is withdrawn with a syringe, the remainder does not spread out and cover the whole oil-water interface. Instead, it condenses to form a lens which is situated between the upper oil phase and lower water phase with finite contact angles. This formation indicates that the water-oil interfacial tension is less than the sum of the small water-microemulsion and oil-microemulsion interfacial tensions. When the solution is gently swirled in a polycarbonate tube, the microemulsion lens can preferentially attach itself to the walls of the container and form a ring along the edge of the tube. At the oil-water interfacial region inside of this ring, there is a single, macroscopically flat surfactant monolayer that is in thermal equilibrium and at the same chemical potential as the surfactant monolayers contained within the surrounding microemulsion ring.

We used x-ray reflectivity to study the statistical fluctuations of this saturated surfactant monolayer, because it is a particularly sensitive probe of structure through and across the liquid interface. Previously, the x-ray reflectivity technique has been used to study the fluctuations of vapor-liquid interfaces and the layering of a liquid crystal at a liquid-solid interface [44, 45, 46, 47, 48]. Before we could apply this technique to the oil-water interface, however, a number of technical issues and details had to be addressed. One problem with scattering from a liquid-liquid surface is that the critical angle for total external x-ray reflection is very small, typically only hundredths of a degree. Such low angles required both tight instrumental resolution and relatively large sample areas to contain the x-ray "footprint" within the area of interest. Another concern is the upper liquid phase itself which attenuates the incident and reflected x-ray beams. To overcome this difficulty, high energy x-rays of wavelength $\lambda = 0.714\,\text{Å}$, corresponding to an energy of 17.4 keV, were used to traverse the upper decane phase. The resultant absorption length was approximately 2.5 cm, which determined the optimal sample size. At this x-ray wavelength, the critical angle for total external reflection from the oil-water interface was measured
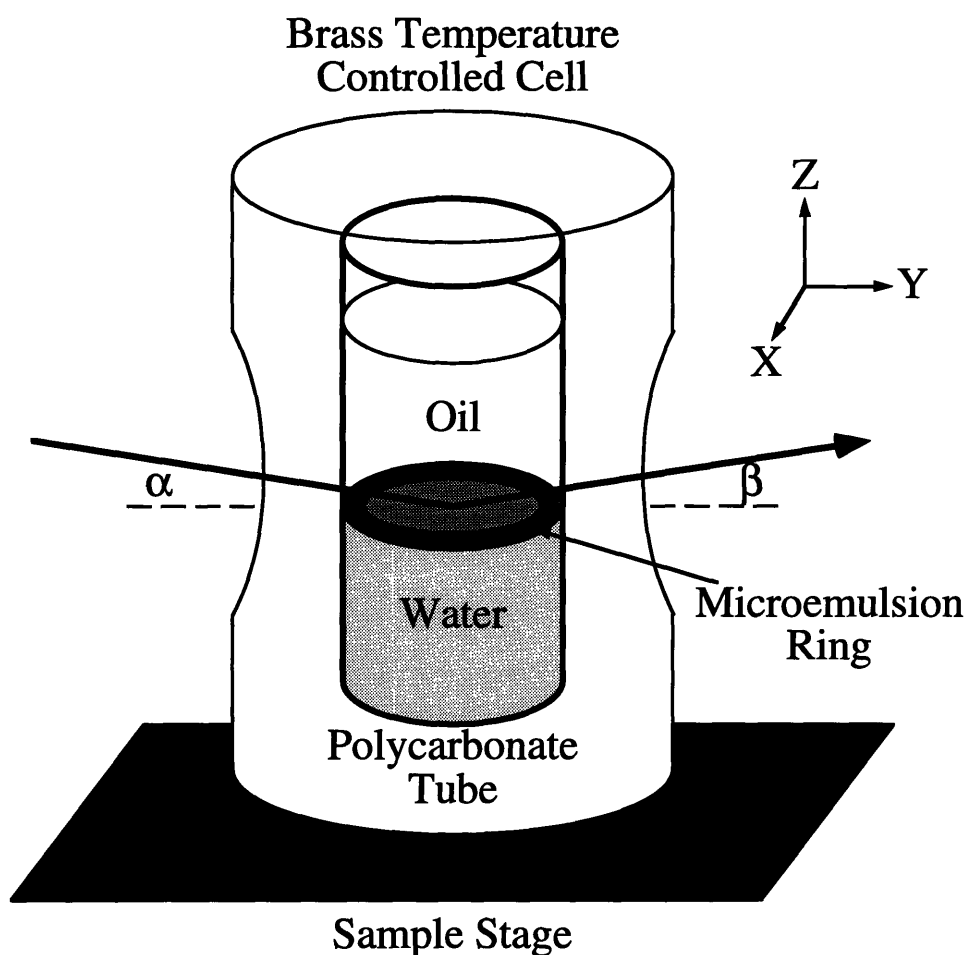
Figure 3-2: Experimental setup for measuring the x-ray scattering.

to be $0.03°$.

The experiments were performed on the X20B beam line at the National Synchrotron Light Source using a specially constructed reflectometer [49]. The experimental setup and scattering geometry are shown in Figure 3-2. The incoming beam was tilted downward by an angle α using the Bragg reflection from a Ge(111) crystal. As the incident angle was changed, the vertical position of the sample stage was adjusted so that the incoming beam always hit the center of the surfactant interface. The detector was located on a second vertical stage that was adjusted so that the x-ray signal scattered at the desired angle β was sampled. A pair of slits located just in front of the sample were used to define the vertical (5 μm) and horizontal (1 mm)

width of the beam and thus the illuminated sample area. The beam footprint on the sample at the critical angle was then small enough to reside completely within the oil-water interfacial region. The collimation of the incident beam corresponded to an angular deviation of only $\Delta\alpha = 1.8 \times 10^{-6}$ radians half-width-at-half-maximum (HWHM). A second pair of slits placed just before the detector defined the vertical angular acceptance to be $\Delta\beta = 1.9 \times 10^{-5}$ radians (HWHM) while leaving the horizontal angular acceptance essentially wide open.

3.2 Scattering Results

By varying both the incident angle α and exit angle β, the scattering signal from the surfactant monolayer can be systematically mapped out. We define Q_z to be the component of the wave vector transfer normal to oil-water interface:

$$Q_z = \frac{2\pi}{\lambda}(\sin\alpha + \sin\beta), \tag{3.1}$$

while Q_y is the component parallel to the interface in the plane of the scattering:

$$Q_y = \frac{2\pi}{\lambda}(\cos\beta - \cos\alpha). \tag{3.2}$$

Due to the large angular acceptance of the instrument in the out-of-plane direction, the measured scattering is essentially integrated over the remaining transverse component Q_x. Figure 3-3 shows some of our raw experimental scattering data from the oil-water interface as a function of Q_y and Q_z.

3.2.1 Specular Reflectivity

The sharply peaked ridge in the scattering at $Q_y = 0$ in Figure 3-3 corresponds to the angular condition $\alpha = \beta$. This ridge thus contains the signal from x-rays specularly reflected off of the oil-water interface. In order to isolate this specular reflectivity component, the background due to small angle scattering from bulk phases and diffuse
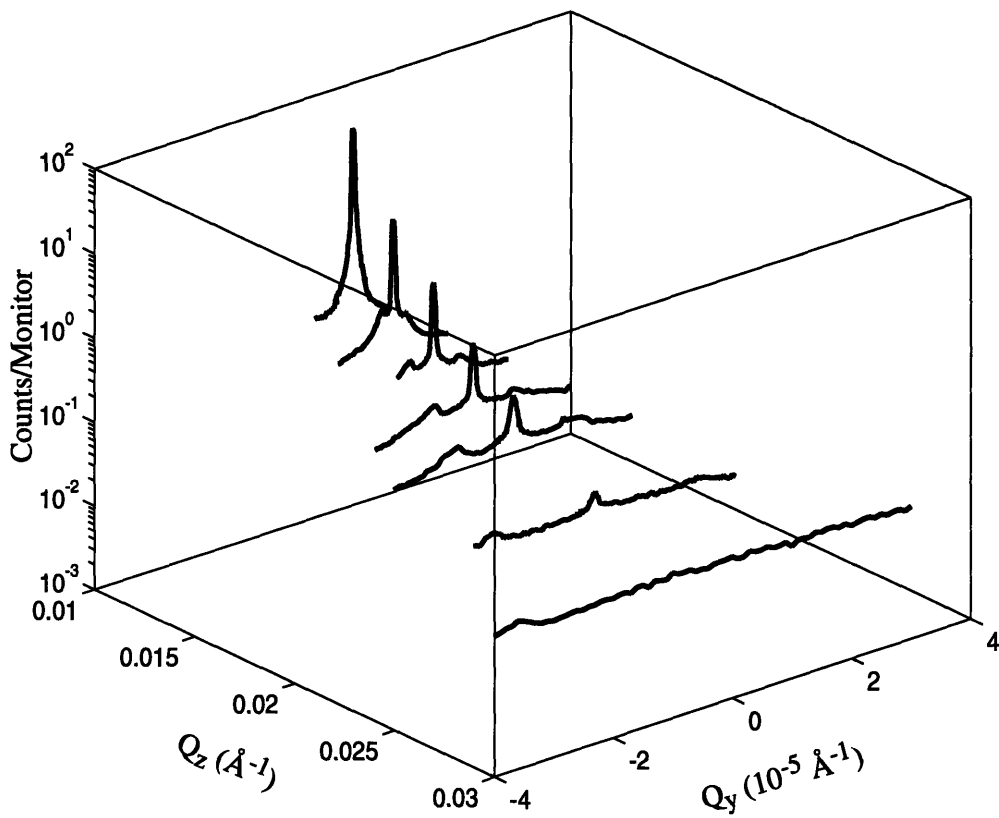
Figure 3-3: Raw x-ray scattering data as a function of Q_y and Q_z.
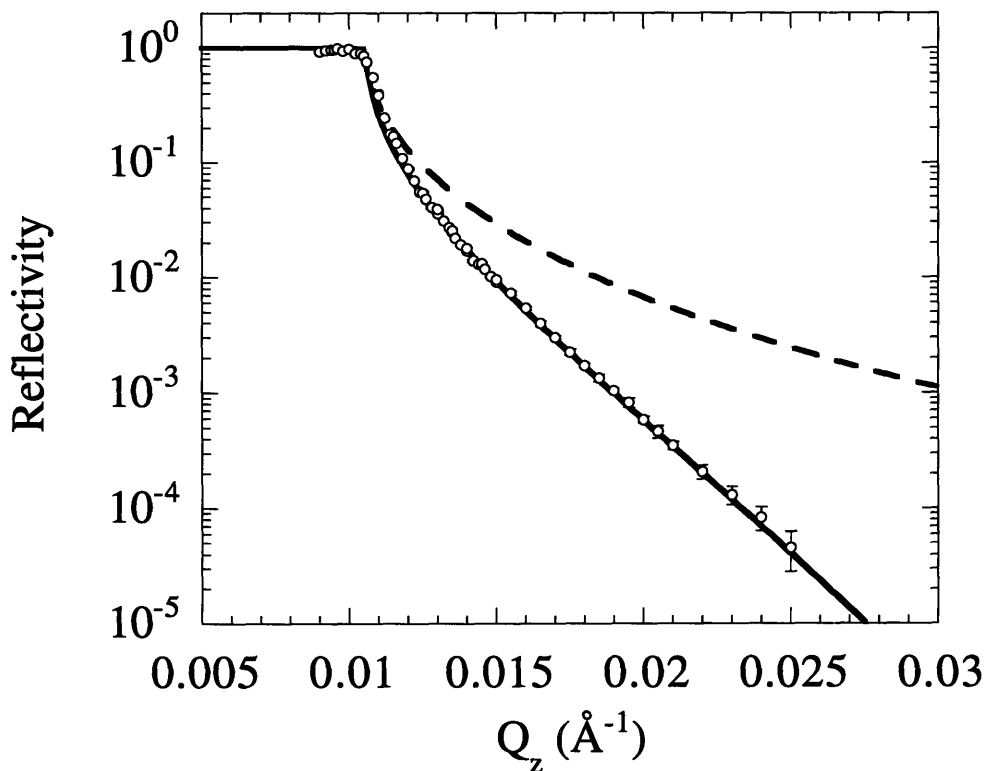
Figure 3-4: Specular reflectivity from the oil-water interface.

scattering from the interface is measured by offsetting the detector arm 100 μm in height. This background term is subtracted from the signal at $Q_y = 0$ and the data is rescaled so that it is equal to unity below the critical angle. The resulting true specular reflectivity is plotted as a function of Q_z in Figure 3-4. The circles represent our data, and the dashed line is the theoretical Fresnel prediction for a perfectly flat interface according to Equation 2.28.

The critical wave vector for total external reflection is measured to be $Q_c = 0.0105\,\text{Å}^{-1}$. For increasing values of Q_z above Q_c, the experimentally measured reflectivity becomes progressively much less than the Fresnel prediction. This rapid decay in the specular reflectivity is due to roughness caused by large thermal fluctuations in the surfactant monolayer at the oil-water interface. In order to determine the interfacial roughness of the monolayer, we use a slightly modified form of Equa-

tion 2.40 to model the specular reflectivity [50, 42]:

$$R(Q_z) = R_F(Q_z) \exp(-\sigma^2 Q_z Q_z^t) \tag{3.3}$$

where σ is the root mean square roughness, and $Q_z^t \simeq \sqrt{Q_z^2 - Q_c^2}$ is the z-component of the wave vector transfer with respect to the lower water phase. Equation 3.3 is slightly superior to Equation 2.40 in the region around the critical edge, but the two expressions are essentially equivalent at large Q_z.

Fitting the measured reflectivity with Equation 3.3 results in the solid line shown in Figure 3-4. The roughness of the interface is determined to be equal to $\sigma = 85 \pm 3\,\text{Å}$. The large value for σ indicates that this surface is indeed quite rough and that fluctuations are important in determining the behavior of the surfactant monolayer at this interface.

3.2.2 Capillary Wave Model

We hypothesize that the large roughness of the oil-water interface can be directly attributed to capillary wave fluctuations in the surfactant monolayer. As previously illustrated in Figure 2-8, the interface is modelled as a height function $z(x, y)$ which describes the deviation of the monolayer away from an average flat surface. A Hamiltonian which incorporates the leading order interfacial tension term and gravitational effects can then be written [51]:

$$\mathcal{H}\{z(x,y)\} = \int dx\, dy \left[\frac{1}{2} g \Delta\eta\, z^2 + \gamma \sqrt{1 + \left(\frac{dz}{dx}\right)^2 + \left(\frac{dz}{dy}\right)^2} \right] \tag{3.4}$$

$$\simeq \gamma A + \frac{1}{2} \int dx\, dy \left[g \Delta\eta\, z^2 + \gamma\, (\nabla z)^2 \right] \tag{3.5}$$

where g is the gravitational acceleration, $\Delta\eta$ is the mass density difference between the upper and lower phases, γ is the interfacial tension, and A is the area of a perfectly flat interface. From Equation 3.5, the surface height-height correlation function can

44

be calculated:

$$\langle z(0)z(r)\rangle \;=\; k_B T \int \frac{d^2\vec{k}}{(2\pi)^2} \frac{e^{i\vec{k}\cdot\vec{r}}}{g\Delta\eta + \gamma k^2} = \frac{k_B T}{2\pi\gamma} \mathrm{K}_0\left(\sqrt{\frac{g\Delta\eta}{\gamma}}\,r\right) \qquad (3.6)$$

where $k_B T$ is the thermal energy, and $\mathrm{K}_0(x)$ is a modified Bessel function of the first kind.

The function $\mathrm{K}_0(x)$ in Equation 3.6 diverges logarithmically for small arguments x. Therefore the correlation function $\langle z(0)\,z(r)\rangle$ increases without bound for small r and so the roughness $\sigma = \sqrt{\langle z(0)^2\rangle}$ is predicted to be infinite. This is a shortcoming of the Gaussian approximation used in Equation 3.5. In fact, at short length scales, the interfacial bending rigidity, higher-order interfacial tension terms, or possibly the molecular spacing between surfactant molecules prevents the ultraviolet divergence. Accordingly, we introduce a length scale r_0 that explicitly cuts off the correlation function:

$$\langle z(0)\,z(r)\rangle = \frac{k_B T}{2\pi\gamma} \mathrm{K}_0\left(\sqrt{g\Delta\eta(r^2 + r_0^2)/\gamma}\right). \qquad (3.7)$$

The cutoff length scale r_0 is then related to the mean square roughness of the interface:

$$\sigma^2 = \frac{k_B T}{2\pi\gamma} \mathrm{K}_0(r_0\sqrt{g\Delta\eta/\gamma}). \qquad (3.8)$$

3.2.3 Diffuse Scattering

We tested the validity of the capillary wave model by analyzing the form of the surface diffuse scattering from the surfactant monolayer. In contrast to specular reflectivity which yields information about the average density variation through the interface, the diffuse scattering is related to the Fourier transform of the correlation function $\langle z(0)\,z(r)\rangle$ and is therefore sensitive to height variations along the surface of the oil-water interface. We measured this scattering by performing a series of transverse scans at several different values of Q_z. In each of these scans, the wave vector transfer is no longer fixed to be normal to the interface; instead, Q_y is systematically varied at constant Q_z by "rocking" the incident angle α and exit angle β. Bulk small angle
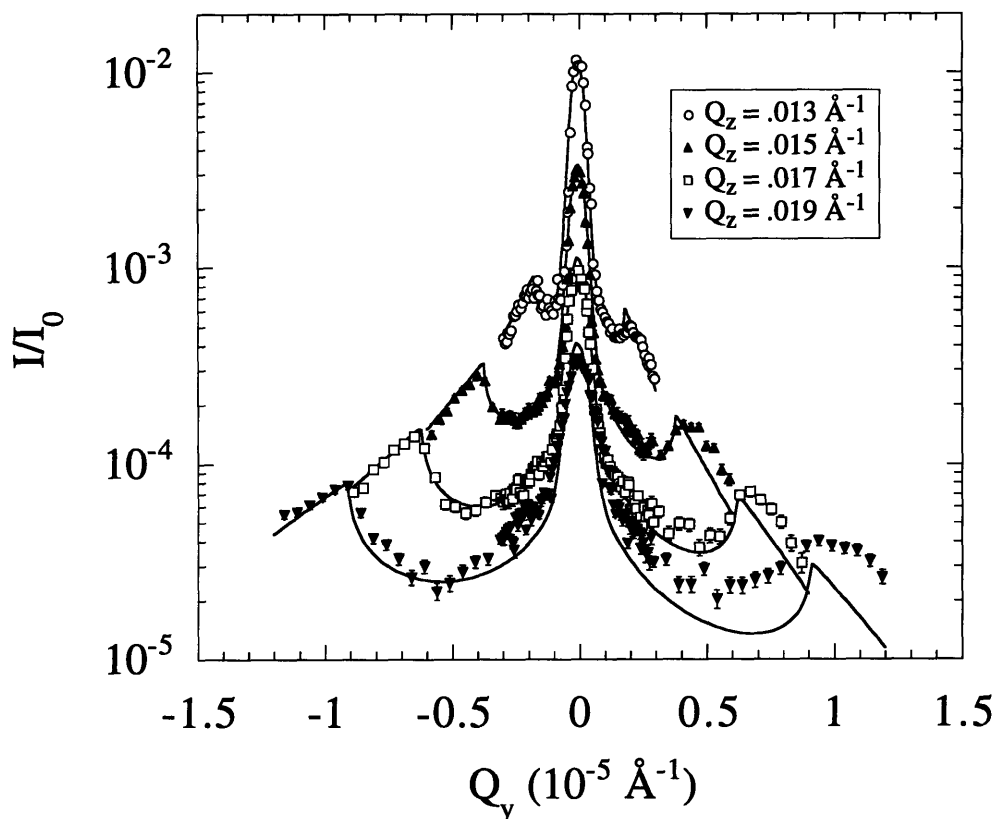
Figure 3-5: Surface scattering from transverse scans.

scattering from the oil-rich and water-rich phases contributes a flat background to these scans. This small angle scattering was measured independently by offsetting the sample vertically so that the beam avoided the interface and traversed only the upper or lower phase. Figure 3-5 shows the measured transverse scans taken at four different Q_z values with the background bulk scattering subtracted out.

The specularly reflected signal accounts for the large central peaks at $Q_y = 0$. The other peaks at nonzero Q_y occur when either α or β is equal to the critical angle. These so-called "Yoneda wings" arise from an enhancement of the electric field at the interface due to an increase in the transmission factors near the critical edge [52]. The general decrease in the scattering intensity with increasing Q_y is due to a reduction in the interfacial area illuminated by the x-rays for larger incident angles α.

We use the distorted wave Born approximation of Equation 2.42 along with the correlation function in Equation 3.7 to calculate the theoretical form of the interfa-

46

cial diffuse scattering arising from capillary waves [41]. Additionally, the interfacial roughness of the surfactant monolayer is fixed to be $\sigma = 85$ Å as determined from the specular reflectivity. Modelling the specular peaks with Gaussian resolution functions and fitting the measured diffuse scattering scans with the single adjustable parameter γ results in the theoretical curves shown as solid lines in Figure 3-5. We find that the diffuse scattering intensities in the Yoneda wings are approximately inversely related to the interfacial tension; the best fit value is given by $\gamma = 0.11 \pm 0.02$ dyne/cm. Although the theoretical lines match the experimental data reasonably well, some discrepancies occur at large values of Q_y and Q_z. These are probably due to the presence of some excess microemulsion phase attached to the sample tube which is causing some spurious scattering at small exit angles β.

3.3   Discussion

The overall agreement between the experimental data and the model predictions in Figure 3-5 indicates that the capillary wave model provides an accurate description for the statistical fluctuations of the interface. The measured interfacial tension γ is very low and is almost three orders of magnitude smaller than that of the bare oil-water interface, indicating the interface is truly saturated with surfactant. We assume that the large reduction in interfacial tension is due to a saturated surfactant monolayer at this oil-water interface. Any structure other than a monolayer is highly unlikely since a bilayer would be energetically unfavorable and any larger structures would drastically affect the form of the observed surface scattering.

We should note that the interfacial tension of the surfactant monolayer is also much smaller than those of the vapor-liquid interfaces measured by previous x-ray reflectivity experiments [44, 45, 46, 47]. The intrinsic width of the diffuse scattering is given by the inverse capillary length:

$$\sqrt{\frac{g\Delta\eta}{\gamma}} = 5.2 \times 10^{-7} \text{Å}^{-1}. \tag{3.9}$$

Since γ is so small, the intrinsic width of the diffuse scattering from the surfactant monolayer is relatively quite large. In fact, the diffuse scattering width is even larger than the transverse resolution of the experiment, $\Delta Q_y = \frac{1}{2} Q_z (\Delta \alpha + \Delta \beta) \simeq 1.5 \times 10^{-7} \, \text{Å}^{-1}$ (HWHM). This indicates that the true specular scattering can be readily distinguished from the diffuse scattering and the instrumental resolution need not be convolved in the calculation of the diffuse scattering. Thus, our measured values for σ and γ represent true intrinsic interfacial properties of the surfactant monolayer and are not dependent upon the instrumental resolution.

The measured interfacial roughness σ and interfacial tension γ are similar to those found in optical studies on this system [13, 53]. Additionally, these values may be used to deduce a cutoff length scale with the bounds $0.5 \, \text{Å} < r_0 < 40 \, \text{Å}$. Unfortunately, the logarithmic dependence in Equation 3.8 prevents us from making a more precise estimate for r_0. This cutoff length scale can, however, be related to an effective bending rigidity κ using the transformation $\kappa \simeq \gamma r_0^2$ which yields the inequality $\kappa < 0.5 \, k_B T$. Because the estimate for the bending rigidity is so low, the associated persistence length for the surfactant monolayer ξ_κ in Equation 1.6 must be quite small. Thus, the very small interfacial tension and bending rigidity of the surfactant monolayer can account for the thermodynamic stability of the middle-phase microemulsion at this temperature.

Chapter 4

Local Geometry of the Surfactant Monolayers in Microemulsions

In the last chapter, we saw that the fluctuations of a surfactant monolayer in equilibrium with a microemulsion are characterized by an extremely low intrinsic interfacial tension and effective bending rigidity. We now turn our attention towards characterizing the complex three-dimensional geometry of the surfactant monolayers contained within the bicontinuous microemulsion phase. We use a contrast variation technique in order to determine the interfacial areas and deduce the curvature of the monolayers. Our small angle neutron scattering results show that the mean curvature of the surfactant film inverts as a function of temperature [54].

4.1   Geometrical Considerations

Figure 4-1 illustrates a representative cross section of the surfactant monolayer in a microemulsion. Because the surfactant film has a finite thickness d, several distinct interfacial regions can be defined: the water-surfactant interfacial area A_w, the oil-surfactant interfacial area A_o, and the surface area A_s measured at the midpoints of the surfactant molecules. When the surfactant monolayer is bent, the three interfacial areas need not be equivalent. These three areas are, however, related to each other through the principal radii of curvature R_1 and R_2 of the monolayer shown in Figure 1-

49
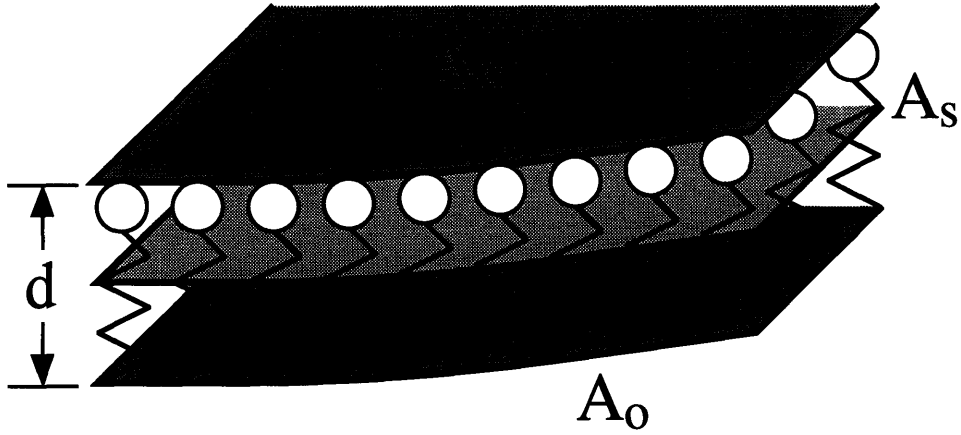
Figure 4-1: Three distinct interfacial areas defined on the surfactant monolayer.

6 [55]. The interfacial areas can be written as surface integrals over the surface through the middle of the surfactant film:

$$A_s = \int 1 \, dS \tag{4.1}$$

$$A_w = \int \frac{(R_1 + \frac{d}{2})(R_2 + \frac{d}{2})}{R_1 R_2} \, dS \tag{4.2}$$

$$A_o = \int \frac{(R_1 - \frac{d}{2})(R_2 - \frac{d}{2})}{R_1 R_2} \, dS. \tag{4.3}$$

These geometrical relations can be simplified using the definitions of the mean curvature C and Gaussian curvature K in Equations 1.3 and 1.4:

$$A_w = A_s \left(1 + dC + \frac{d^2}{4} K \right) \tag{4.4}$$

$$A_o = A_s \left(1 - dC + \frac{d^2}{4} K \right). \tag{4.5}$$

Equations 4.4 and 4.5 imply that if the surfactant monolayer preferentially curves towards either the water or oil phase, there will be a significant splitting in the water-surfactant and oil-surfactant interfacial areas depending upon the mean curvature of

50

Figure 4-2: Differences in the interfacial areas for curved phases.

the film. This difference in the interfacial areas for some simple examples is illustrated in Figure 4-2. For a spherical oil-in-water microemulsion, the interfacial area on the water side of 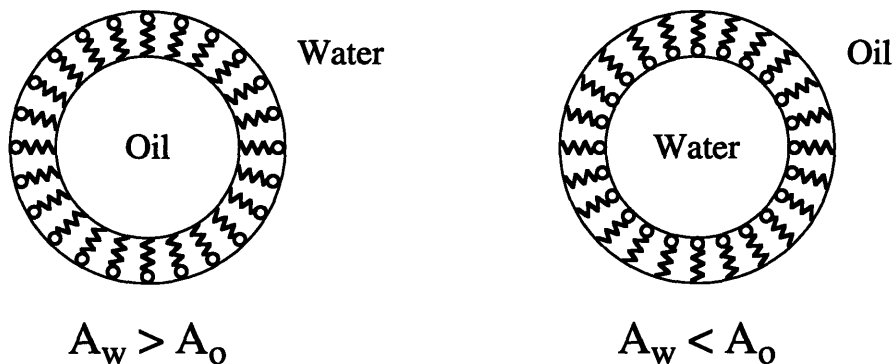the monolayer is larger than the interfacial area on the oil side of the monolayer. On the other hand, the water interfacial area is less than the oil interfacial area in a reverse water-in-oil microemulsion. For lamellar or bicontinuous microemulsions with no preferential curvature, the two interfacial areas should be approximately the same. Thus, differences in the interfacial areas of the surfactant film can be used to deduce information about the overall curvatures of the monolayers in the microemulsion structure [56, 57].

4.2 Contrast Variation

Experimentally determining the geometry of the surfactant monolayer becomes a matter of measuring the various interfacial areas of the surfactant film. We used contrast variation in conjunction with small angle neutron scattering (SANS) to highlight and measure the areas of the different interfaces [58]. The microemulsion containing the surfactant monolayers is a ternary solution composed of water, oil, and surfactant, and its scattering length density can be linearly decomposed into three parts [59, 60]:

$$\rho(\vec{r}) = \rho_w \phi_w(\vec{r}) + \rho_o \phi_o(\vec{r}) + \rho_s \phi_s(\vec{r}). \qquad (4.6)$$

The scattering length densities of the pure water, oil, and surfactant are denoted ρ_w, ρ_o, and ρ_s, respectively, while the local volume fractions of the three components are given by $\phi_w(\vec{r})$, $\phi_o(\vec{r})$, and $\phi_s(\vec{r})$. Assuming that the microemulsion is an incompressible liquid, the local volume fractions satisfy the following constraint:

$$\phi_w(\vec{r}) + \phi_o(\vec{r}) + \phi_s(\vec{r}) = 1. \tag{4.7}$$

To obtain the scattering function in terms of the scattering length densities and local volume fractions of the three phases, we substitute Equation 4.6 for the scattering length density in Equation 2.4. Using Equation 4.7 to eliminate various cross terms, we arrive at the following expression:

$$\begin{aligned}
S(\vec{Q}) &= (\rho_w - \rho_o)(\rho_w - \rho_s)\chi_{ww}(\vec{Q}) + (\rho_o - \rho_w)(\rho_o - \rho_s)\chi_{oo}(\vec{Q}) + \\
&\quad (\rho_s - \rho_w)(\rho_s - \rho_o)\chi_{ss}(\vec{Q}).
\end{aligned} \tag{4.8}$$

The partial structure factors $\chi_{ij}(\vec{Q})$ where $i, j = \{w, o, s\}$ are defined by the Fourier transforms of the appropriate correlation functions:

$$\chi_{ij}(\vec{Q}) = \frac{1}{V} \int \langle \phi_i(0)\, \phi_j(\vec{r}) \rangle\, e^{i\vec{Q}\cdot\vec{r}}\, d^3\vec{r}. \tag{4.9}$$

Note that Equation 4.8 is written in terms of the three structure factors $\chi_{ww}(\vec{Q})$, $\chi_{oo}(\vec{Q})$, and $\chi_{ss}(\vec{Q})$. All the other cross correlations $\chi_{ij}(\vec{Q})$ where $i \neq j$ are dependent upon these three direct correlations. For instance, the water-surfactant cross correlation term that has been used to analyze earlier neutron scattering experiments is equivalent to the combination [56, 57]:

$$\chi_{ws}(\vec{Q}) = \frac{1}{2}\left[\chi_{oo}(\vec{Q}) - \chi_{ww}(\vec{Q}) - \chi_{ss}(\vec{Q})\right]. \tag{4.10}$$

The three structure factors $\chi_{ww}(Q)$, $\chi_{oo}(Q)$, and $\chi_{ss}(Q)$ can all be independently measured by varying the water scattering length density ρ_w and the oil scattering length density ρ_o. If the oil scattering length density is matched to the surfactant

scattering length density $(\rho_o = \rho_s)$, the oil-oil and surfactact-surfactant correlation functions will not contribute to Equation 4.8. In this case, the scattering function $S(Q)$ is proportional to only the water-water partial structure factor $\chi_{ww}(Q)$. Similarly, when the contrast of the water is matched to the surfactant $(\rho_w = \rho_s)$, the scattering is determined by simply the correlations between the oil regions $\chi_{oo}(Q)$. The third possibility is to isolate the surfactant-surfactant partial structure $\chi_{ss}(Q)$ by setting the water and oil scattering length densities equal to each other $(\rho_w = \rho_o)$.

The advantage of using neutrons as a scattering probe is that the scattering length densities of both the water and oil phases can be easily varied by substituting deuterium atoms for hydrogen atoms. This isotopic substitution effectively changes the contrast of the system because the coherent neutron scattering length of deuterium is $b_D = 6.7 \times 10^{-5}\,\text{Å}$ while the coherent neutron scattering length of hydrogen is actually negative $b_H = -3.7 \times 10^{-5}\,\text{Å}$ [61]. Thus, the scattering length densities of D_2O and perdeuterated oil are vastly different from that of H_2O and hydrogeneous oil. As shown in Figure 4-3, the water-water, oil-oil, and surfactant-surfactant partial structure factors of a microemulsion can then be isolated and determined by systematically replacing the water and oil with their deuterated counterparts. Each of the three contrasts pictured describes essentially a two-phase medium. Scattering from the water-water contrast is related to the water-surfactant interfacial area A_w, while scattering from the oil-oil contrast depends upon the oil-surfactant interfacial area A_o. Scattering from the surfactant-surfactant contrast highlights only the surfactant film and is related to the surface area A_s.

4.3 Small Angle Neutron Scattering

We used a microemulsion system consisting of water, octane, and tetraethylene glycol monodecyl ether $(C_{10}E_4)$. Figure 4-4 shows the phase diagram of this system as a function of temperature and surfactant volume fraction ϕ_s when the water and octane volume fractions are equal to each other $(\phi_w = \phi_o)$. The temperature at which the hydrophilicity and hydrophobicity of the surfactant is balanced is approximately

Water-Water Contrast
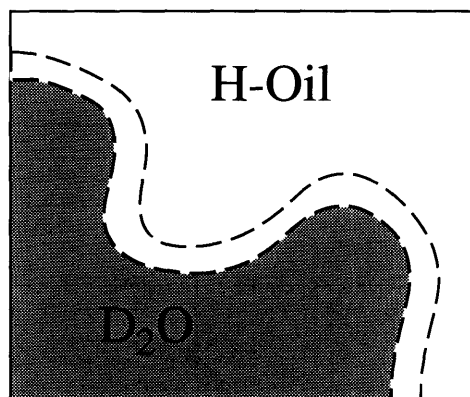
Oil-Oil Contrast
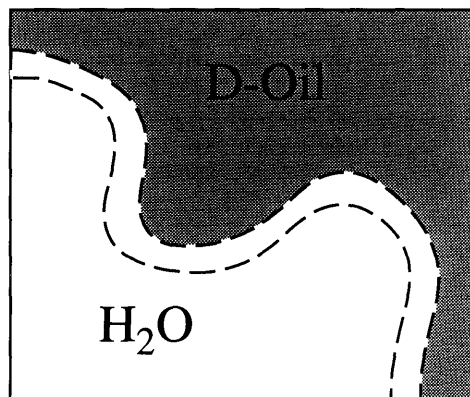
Surfactant-Surfactant
Contrast
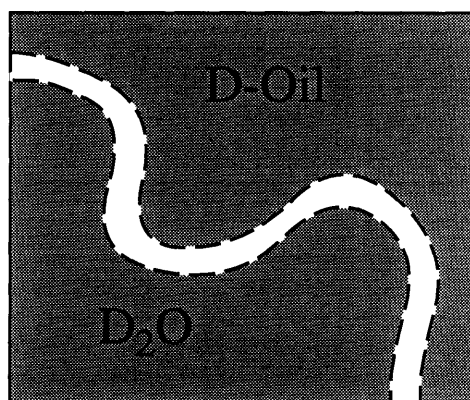
Figure 4-3: Contrast variation can highlight different regions in the microemulsion.

Figure 4-4: Phase diagram for the H$_2$O-octane-C$_{10}$E$_4$ system with equal volume fractions of water and oil.

55

given by the location of the intersection of the three-phase region (3Φ) with the single phase region (I) in the phase diagram (T $\approx$ 25 °C) [62]. At lower temperatures, a microemulsion phase coexists with an excess oil phase ($\underline{2}\Phi$), while at higher temperatures, a microemulsion coexists with an excess water phase ($\overline{2}\Phi$) as described in Section 1.2. A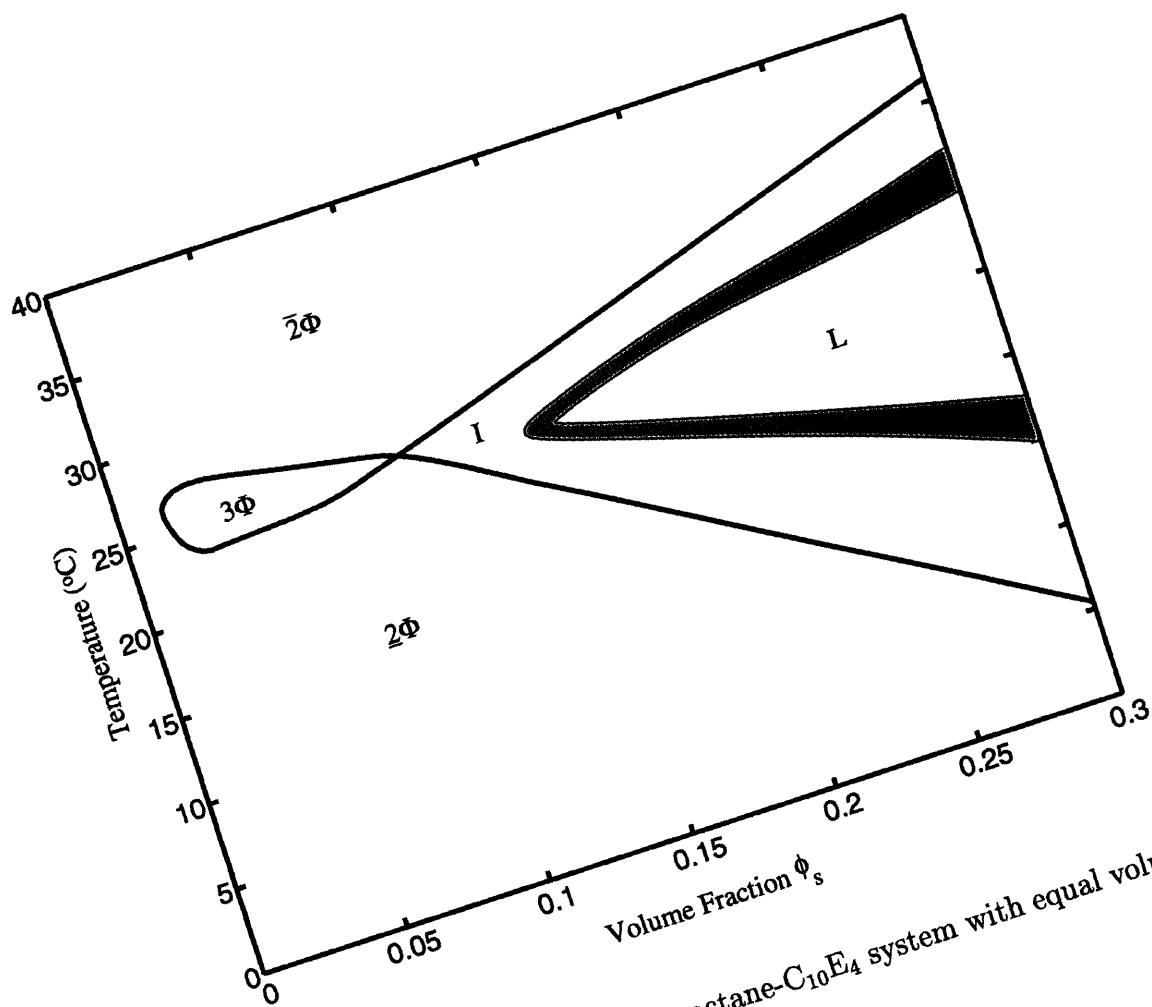t large surfactant concentrations ϕ_s, a lamellar phase (L) becomes thermodynamically stable. The lamellar phase coexists with an isotropic microemulsion phase within the shaded regions.

H_2O (reverse-osmosis and polished with a Millipore Milli-Q system to 18 MΩ-cm), D_2O (Cambridge Isotope Laboratory, 99.9%), octane (Aldrich, 99+%), perdeuterated octane (Cambridge Isotope Laboratory, 99%), and $C_{10}E_4$ (Fluka, 97%) were used to prepare the samples for this set of experiments. These ingredients were weighed with an accuracy of 0.1% and mixed to yield a series of solutions where the scattering length densities of the water and oil varied between $-0.1 \times 10^{-6} < \rho_w, \rho_o < 6.5 \times 10^{-6}\,\text{Å}^{-2}$. The samples were measured in a range of temperatures spanning the bicontinuous microemulsion and lamellar phase regions. The small angle neutron scattering data were taken on the 30 m NSF SANS instrument at the National Institute of Standards and Technology (wavelength $\lambda = 6.0$ Å and wavelength spread $\Delta\lambda/\lambda = 15\%$) and the H9B diffractometer at Brookhaven National Laboratory ($\lambda = 5.0$ Å and $\Delta\lambda/\lambda = 10\%$). This data was corrected for background scattering and reduced to an absolute scale as detailed in Section 2.2.

The phase diagrams for the samples were found to be shifted downward in temperature by up to 2 °C upon the substitution of deuterium for hydrogen. The temperature shift is due to the mass difference between deuterium and hydrogen and has been seen in studies on similar microemulsion systems [63]. To take this isotopic effect into account, the different solutions in a contrast-varied series were measured in the same relative position within their respective phase diagrams. Three of the measured scattering curves were used to determine the three partial structure factors. The other scattering curves were found to be related to the partial structure factors according to Equation 4.8. The consistency between the various scattering curves indicate that aside from the temperature shift in the phase diagrams, there is very
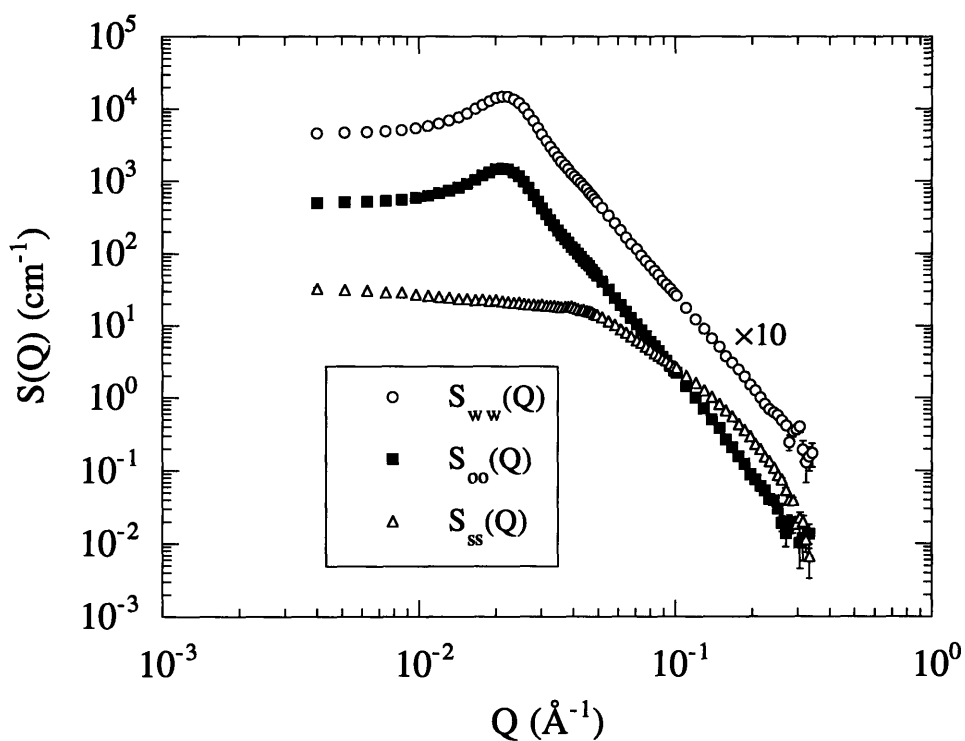
Figure 4-5: SANS curves for the three different contrasts.

little effect of isotopic substitution on the structure of the monolayers.

Let us first consider the scattering results for a microemulsion consisting of 13.2% $C_{10}E_4$, 43.4% water, and 43.4% octane by volume. After subtracting the background due to incoherent scattering, the three measured structure factors corresponding to a temperature $T = 24.0\,^\circ\mathrm{C}$ are plotted in Figure 4-5. The water-water correlations in $S_{ww}(Q)$ and the oil-oil correlations in $S_{oo}(Q)$ are very similar to each other, and both scattering curves show a broad peak near $Q_{max} \approx 0.02\,\text{Å}^{-1}$. From the location of this peak, we get a rough estimate for the size of the water and oil domains in this microemulsion: $D \simeq \pi/Q_{max} = 145 \pm 5\,\text{Å}$.

The thickness and various interfacial areas of the surfactant monolayer can be determined from the behavior of the scattering functions at relatively large values of Q. In principle, the structure factors $\chi_{ww}(Q)$ and $\chi_{o}o(Q)$ are related to the interfacial areas A_w and A_o according to Equation 2.19. However, because the water and oil molecules penetrate significantly into the surfactant film, the interfaces between the

57

surfactant film and the water and oil phases are not perfectly sharp. In order to account for the diffuse water-surfactant and oil-surfactant interfaces, Equation 2.19 is modified to include the effects of solvent penetration [63]:

$$\chi_{ww}(Q) = 2\pi \frac{A_w}{V} \frac{e^{-\sigma_w^2 Q^2}}{Q^4} \qquad (4.11)$$

$$\chi_{oo}(Q) = 2\pi \frac{A_o}{V} \frac{e^{-\sigma_o^2 Q^2}}{Q^4}. \qquad (4.12)$$

The penetration length of the water into the monolayer is equal to $2\sigma_w$ and the penetration length of the oil is given by $2\sigma_o$. Thus, when the penetration of water or oil into the surfactant monolayer is large, the corresponding structure factor decays much more rapidly than predicted that by Equation 2.19. Also, because the water-surfactant and oil-surfactant interfaces are diffuse, the transverse profile of the surfactant monolayer can be modelled with a Gaussian function. Then at large wave vectors, the scattering from the film takes the simple form:

$$\chi_{ss}(Q) = 2\pi \phi_s^2 \frac{V}{A_s} \frac{e^{-d^2 Q^2/2\pi}}{Q^2} \qquad (4.13)$$

where the effective thickness of the surfactant film is $d = (V/A_s)\phi_s$.

We use Equation 4.13 to fit the experimental scattering curve $S_{ss}(Q)$ at wave vectors $Q > 0.1 \, \text{Å}^{-1}$. The thickness of the surfactant film is found to be $d = 13.8 \pm 0.7 \, \text{Å}$ and the surface to volume ratio is $A_s/V = 0.0095 \pm 0.0001 \, \text{Å}^{-1}$. This surface area corresponds to an interfacial area per surfactant molecule of about 41 Å^2. The measured structure factors $S_{ww}(Q)$ and $S_{oo}(Q)$ are analyzed using Equations 4.11 and 4.12, and the scattering curves and their corresponding fits are shown in Figure 4-6. By plotting the data in this fashion, the slopes of the fitted lines are proportional to the water and oil penetration lengths while the locations of the intercepts are related to the interfacial areas. The best fit parameters for the water-surfactant interface are $\sigma_w = 2.0 \pm 0.3 \, \text{Å}$ and $A_w/V = .01106 \pm .00005 \, \text{Å}^{-1}$. The corresponding values for the oil-surfactant interface are $\sigma_o = 3.8 \pm 0.3 \, \text{Å}$ and $A_o/V = .01069 \pm .00005 \, \text{Å}^{-1}$.

There are several sources of error that appear in the determination of the in-
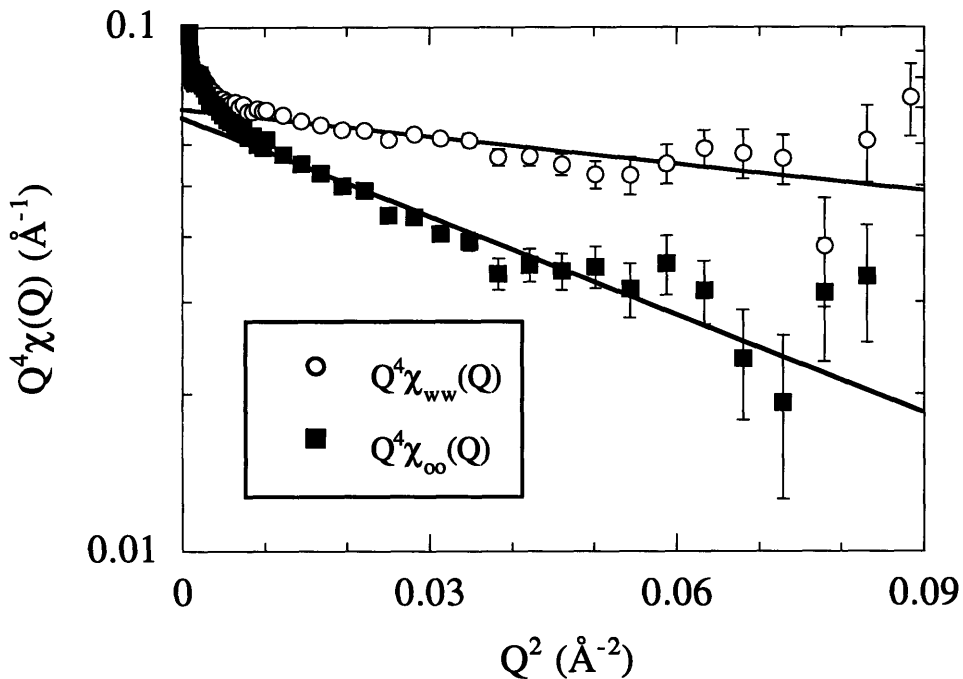
Figure 4-6: Large Q behavior of the water-water and oil-oil scattering curves.

terfacial areas A_w and A_o. The transmission factors used to calibrate the scattering curves are typically only accurate to about 5%. Fortunately, the invariant $(1/2\pi^2)\int S(Q)\,4\pi Q^2 dQ$ can be used to normalize the measured scattering in order to effectively factor out this uncertainty. For a two-phase medium with a diffuse interface, the invariant is equal to:

$$\frac{1}{2\pi^2}\int S(Q)\,4\pi Q^2 dQ = (\rho_1 - \rho_2)^2 \left[\phi_1\phi_2 - \frac{1}{\sqrt{\pi}}\left(\frac{A}{V}\right)\sigma\right]. \qquad (4.14)$$

Thus, using the invariant to normalize the scattering also eliminates any errors associated with lowering of the scattering length density of the oil phase due to dissolved surfactant monomers.

The effects of the finite instrumental resolution are also not negligible. The finite collimation of the instrument is relatively unimportant at large Q, but the large wavelength spread of the neutrons causes a significant broadening of the scattering curve [64]. Multiple coherent scattering in the sample also smears the observed scat-

tering pattern [65]. A calculation that includes these effects indicates that although the functional form of the scattering in Equations 4.11 and 4.12 remains relatively unchanged, the apparent values for the interfacial areas A_w and A_o are elevated by a few percent. However, because the structure factors $S_{ww}(Q)$ and $S_{oo}(Q)$ have very similar magnitudes and shapes, the effects of smearing are nearly equal in the two curves. Thus, by taking the following ratio to calculate the mean curvature of the surfactant monolayer, corrections due to smearing are virtually eliminated:

$$C = \frac{1}{d} \cdot \frac{A_o - A_w}{A_o + A_w} = (-1.2 \pm 0.5) \times 10^{-3}\,\text{Å}^{-1}. \qquad (4.15)$$

Compared with the inverse of the domain size in the microemulsion $1/D \approx 0.007\,\text{Å}^{-1}$, the mean curvature of the surfactant monolayer is very small. These samples were measured near the temperature where the hydrophilicity and hydrophobicity of the surfactant are balanced. Thus, the surfactant monolayers in the microemulsion preferentially curve neither towards the water nor towards the oil phase, resulting in the nearly zero mean curvature.

4.4　Temperature Dependence

As discussed in Section 1.2 and shown in Figure 4-4, varying the temperature has a large effect on the interaction strengths and phase behavior of this microemulsion system. There should also be corresponding changes in the structure and geometry of the surfactant monolayers within the microemulsion phase [66]. We investigated the effect of temperature changes on microemulsion samples consisting of 20.0% $C_{10}E_4$, 40.0% water, and 40.0% octane. The scattering from a contrast-varied series of solutions were measured at various temperatures in the range $16\,°\text{C} < T < 31\,°\text{C}$. By fitting the partial structure factors at each temperature, the interfacial areas of the surfactant film were determined and used to calculate the mean curvature of the monolayer. The mean curvature is shown as a function of temperature in Figure 4-7 along with the isotropic-lamellar coexistence regions and phase separation boundaries.
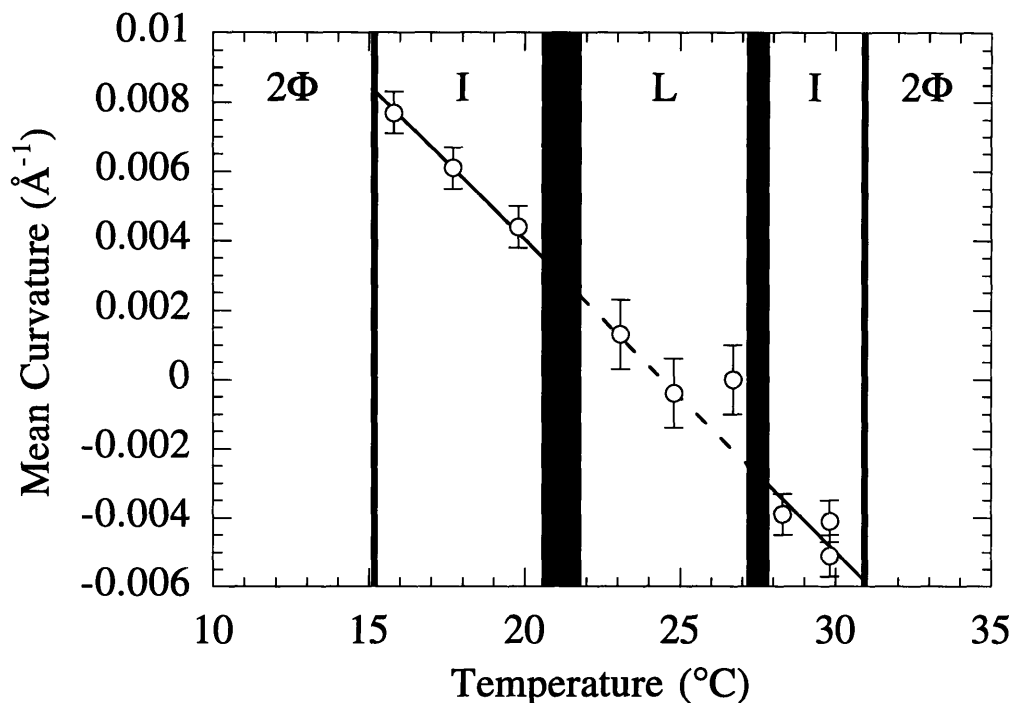
Figure 4-7: Mean curvature of the surfactant monolayer as a function of temperature.

Figure 4-7 shows that the mean curvature depends almost linearly with temperature in the isotropic microemulsion phases: $C = \delta (T - T_0)$ where $\delta = 9.0 \times 10^{-4} \text{\AA}^{-1}/°C$ and $T_0 = 24.4 °C$. The surfactant film is curved towards the oil at the lower temperatures and curved towards the water at the higher temperatures. There is some indication that the mean curvature of the surfactant monolayers within the lamellar phase is also changing with temperature. The errors for measuring the mean curvature of lamellar phases are greater because the presence of quasi-long range order leads to anisotropic averaging of the experimental scattering patterns. Nevertheless, it is clear that the mean curvature of the lamellar phase is much closer to zero than that of the neighboring isotropic phases.

The measurements of the water penetration length ($\sigma_w = 2.0 \text{\AA}$) and the oil penetration length ($\sigma_o = 3.8 \text{\AA}$) into the surfactant monolayer do not change considerably for the different solutions. We initially expected water molecules to hydrogen bond with oxygen atoms all along the length of the hydrophilic head group of the surfactant. The low penetration of the water compared to the oil indicates that perhaps the

surfactant head groups form a compact molecular structure while the surfactant tails are free to intedigitate with the oil. This interaction may explain why the surfactant exhibits a greater critical micellar concentration in the oil than in water.

Equations 4.4 and 4.5 suggest that the Gaussian curvature K of the monolayers may be determined by careful measuring the three interfacial areas A_w, A_o, and A_s. Unfortunately, the difference in the three interfacial areas due to the Gaussian curvature term is much smaller than the splitting due to the mean curvature. Thus, in order to determine K, the three interfacial areas need to be measured very accurately and effects due to smearing would have to be carefully corrected. Another possible way to measure the Gaussian curvature is to use the Q^{-6} correction term to Porod's law in Equation 2.17 [67]. But in most microemulsion systems, the diffuse nature of the interfaces seems to mask any effects the curvature correction might have on the form of the scattering. At present, measuring the higher-order curvature statistics of the monolayer appears to be very difficult due to intrumental resolution effects and experimental errors.

Information about the interfacial areas A_w and A_o has, however, enabled us to quantify the small mean curvature of the surfactant monolayers in the isotropic microemulsion and lamellar phases. Although the topology of the surfactant film in the bicontinuous microemulsion phase is quite complex, we see a clear inversion in the mean curvature about the expected hydrophilic-hydrophobic balance temperature. Contrast variation in conjuction with small angle neutron scattering thus allows us to obtain detailed information about the local geometry of the surfactant monolayers in solution.

Chapter 5

Bulk and Surface Correlations in Microemulsions

The surfactant monolayers in a bicontinuous microemulsion are very disordered and separate oddly-shaped water and oil regions. In this chapter, we consider how to quantitatively measure the size of the water and oil domains and characterize the amount of disorder in the structure of the microemulsion. We also investigate whether the fluctuations of the surfactant monolayers in a microemulsion near a solid interface are similar to those inside the bulk phase.

5.1 Ginzburg-Landau Theory

In Section 1.4, we saw how the surfactant monolayers in a microemulsion could be described by an effective interfacial Hamiltonian. Here we motivate a Ginzburg-Landau theory that is analytically solvable and can be used to make quantitative predictions about the behavior of the surfactant monolayers. We represent the local concentration difference between water and oil in the microemulsion by a scalar field $\psi(\vec{r})$. By considering the rotational and translational symmetries of the microemulsion, a Ginzburg-Landau Hamiltonian can be written in terms of powers of ψ and its

gradients. We initially consider the simple form:

$$\mathcal{H}_0 \{\psi(\vec{r})\} = \int \left[a_0 \psi^2 + a_2 (\nabla \psi)^2 + a_4 (\nabla^2 \psi)^2 \right] d^3 \vec{r}. \tag{5.1}$$

Because there is a macroscopic amount of internal surfactant interfaces separating the water and oil regions, low energy spatial variations in the order parameter $\psi(\vec{r})$ are necessary in order to describe the microemulsion. Gradient interactions are therefore generally favorable and are associated with a negative coefficient in the Ginzburg-Landau expansion ($a_2 < 0$). The Laplacian interaction term corresponding to the parameter a_4 is then required for thermodynamic stability. Because Equation 5.1 is harmonic, the bulk correlation function can be easily calculated analytically:

$$\langle \psi(0)\, \psi(r) \rangle = \exp(-r/\xi_b) \cdot \frac{\sin(2\pi r/d_b)}{(2\pi r/d_b)}. \tag{5.2}$$

The parameter associated with the oscillatory component in Equation 5.2 is

$$d_b = 2\pi \left[\frac{1}{2} \left(\frac{a_0}{a_4} \right)^{\frac{1}{2}} - \frac{1}{4} \frac{a_2}{a_4} \right]^{-\frac{1}{2}} \tag{5.3}$$

and can be considered the characteristic size of the water and oil domains in the microemulsion. The other parameter describing the exponential decay is given by

$$\xi_b = \left[\frac{1}{2} \left(\frac{a_0}{a_4} \right)^{\frac{1}{2}} + \frac{1}{4} \frac{a_2}{a_4} \right]^{-\frac{1}{2}} \tag{5.4}$$

and is the length scale over which the water and oil domains are correlated. This simple description therefore characterizes the bulk microemulsion in terms of two distinct lengths scales: a domain size d_b and correlation length ξ_b.

Ginzburg-Landau theory can also be used to predict the structure of the microemulsion near an interface [68, 69, 70]. The presence of a flat planar surface at $z = 0$ gives rise to surface fields that are expressed as:

$$\mathcal{H}_s = \int \left[s_1 \psi(x, y, 0) + s_1' \frac{\partial \psi}{\partial z}(x, y, 0) + s_2 \psi^2(x, y, 0) \right] dx\, dy. \tag{5.5}$$

64

The structure of the microemulsion is given by minimizing the Hamiltonian in Equation 5.1 with the boundary condition terms in Equation 5.5. We find that the profile of the order parameter in the microemulsion depends upon the distance z away from the interface and is of the following form:

$$\langle \psi(z) \rangle \sim \exp(-z/\xi_s) \cdot \cos(\frac{2\pi z}{d_s} + \varphi). \tag{5.6}$$

The surface domain size d_s describes the oscillatory component of the profile and should be identical to the corresponding bulk parameter d_b. Similarly, the surface correlation length ξ_s associated with the exponential decay term in Equation 5.6 should also be equal to the bulk correlation length ξ_b. The phase factor φ is an additional parameter that is needed to accomodate relative differences in the surface field strengths s_1, s_1', and s_2. In other words, the boundary conditions on the value of the order parameter at the interface $\langle \psi(0) \rangle$ and its first derivative $\langle \psi'(0) \rangle$ will determine the phase factor φ.

5.2   Bulk SANS

We use small angle neutron scattering to determine the bulk domain sizes and correlation lengths in microemulsion systems. Figure 5-1 shows a small angle neutron scattering measurement of a ternary microemulsion consisting of 13.2% $C_{10}E_4$, 43.4% D_2O, and 43.4% octane at $T = 23\,°C$. This data was taken on the 30m NG7 SANS instrument at the National Institute of Standards and Technology (NIST) with wavelength $\lambda = 5.0$ Å and wavelength spread $\Delta\lambda/\lambda = 14\%$. The experimental scattering data is almost identical to the water-water scattering function $S_{ww}(Q)$ previously measured in Figure 4-5. We use the bulk correlation function derived in Section 5.1 to interpret our scattering results. The theoretical form for the scattering associated with this bulk correlation function is given by [71]:

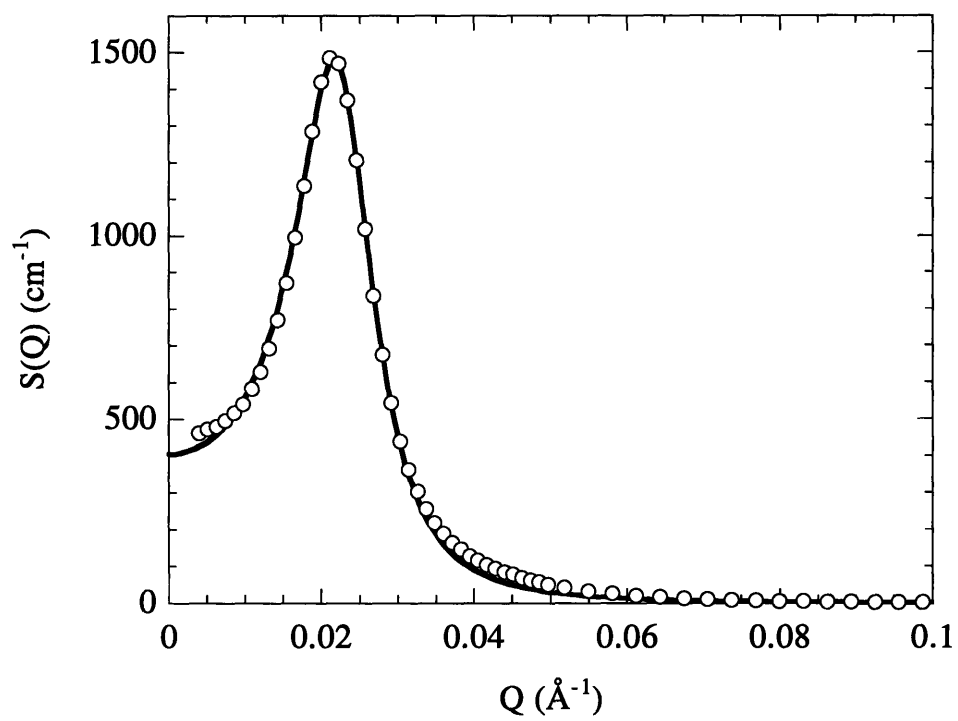$$S(Q) = (2\pi)^3 \frac{\frac{1}{2}k_B T}{a_0 + a_2 Q^2 + a_4 Q^4}. \tag{5.7}$$

65

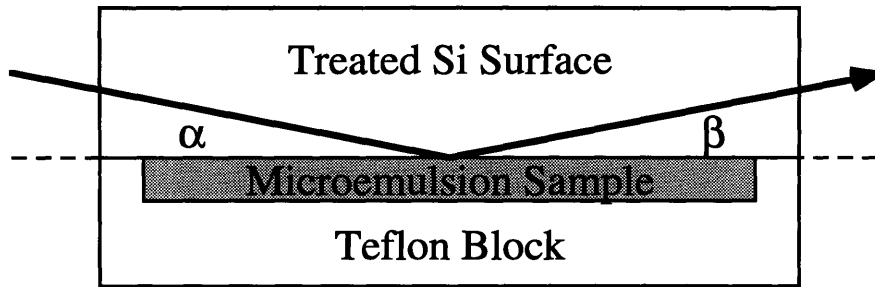Figure 5-1: Small angle neutron scattering from the bulk microemulsion.

Figure 5-2: Experimental setup for reflection from the silicon-microemulsion interface.

Equation 5.7 is convoluted with the instrumental resolution function and fitted to the measured scattering from the microemulsion. The resulting fit is shown as the solid line in Figure 5-1 and corresponds to a bulk domain size $d_b = 278 \pm 2$ Å and a correlation length $\xi_b = 168 \pm 7$ Å. The general agreement between the theoretical prediction of Equation 5.7 and the experimental data in this limited scattering regime seems to indicate that the Ginzburg-Landau theory adequately describes the bulk behavior of the microemulsion. The experimental errors associated with this measurement can be attributed to smearing effects due to the relaxed collimation and wavelength spread of the neutron beam [64].

5.3   Neutron Reflectivity

We next tested the prediction from the simple Ginzburg-Landau theory that the bulk and surface length scales in the microemulsion are equivalent to each other by investigating the interfacial structure of the microemulsion induced by a flat solid surface. We used neutron reflectivity to determine the interfacial profile of the microemulsion near the solid-liquid interface. Our experiments were performed on the BT7 diffractometer in the NIST reactor with the sample cell and scattering geometry shown in Figure 5-2. The liquid microemulsion sample was sandwiched between a single-crystal silicon block and a Teflon holder. A monochromated neutron beam with wavelenth $\lambda = 2.37$ Å and wavelength spread $\Delta\lambda/\lambda = 1\%$ was sent through the silicon block at

an incident angle α. Because silicon is almost transparent to neutron radiation, there was very little attenuation of the neutron beam as it traversed the solid silicon. The portion of the beam that scattered off the solid-liquid interface with an exit angle β was subsequently measured with a He^3 detector.

It was necessary to study the silicon-microemulsion interface because the BT7 reflectometer employs a horizontal scattering geometry and cannot be used to probe free liquid surfaces. One advantage of our experimental setup is that it eliminated problems due to sample evaporation that were present in an earlier reflectivity study [72]. Another advantage of studying the solid-liquid interface is that we are able to treat the silicon surface in order to systematically vary the surface potential fields. For this experiment, 1,1,1,3,3,3-hexamethyldisilizane was used to coat the silicon with a chemisorbed monolayer in order to make it strongly hydrophobic.

Figure 5-3 shows the rocking curve taken at total wave vector transfer $Q = 0.024 \, \text{Å}^{-1}$ for a microemulsion with the same volume concentrations and at the same temperature as the bulk sample in Figure 5-1. This measurement shows the sharply-peaked specular reflectivity component at $\alpha = 0.23°$ in addition to a broad background due to small angle scattering from the bulk of the microemulsion. We separate the specular reflectivity component by subtracting the average background measured by tilting the sample 0.1° in both directions. The reflectivity curve obtained in this fashion is plotted as a function of wave vector transfer Q in Figure 5-4. The circles represent the measured data points, and the dashed line shows the expected smooth decay if the microemulsion had not exhibited any surface structure. In order to obtain a measurable critical reflection edge, D_2O and a mixture of hydrogenous and perdeuterated octane were used to prepare the microemulsion sample. The critical reflection edge ($Q_c \approx 0.011 \, \text{Å}$) in Figure 5-4 corresponds to an average neutron scattering length density in the microemulsion of $\rho = 4.3 \times 10^{-6} \, \text{Å}^{-2}$.

Due to an absorbed surfactant monolayer at the hydrophobic silicon surface, there is an effective interfacial roughness of 7 Å at the silicon-microemulsion interface. In order to model our experimental reflectivity data, we use the surface profile derived in Equation 5.6. We divide this profile into many small layers and calculate the
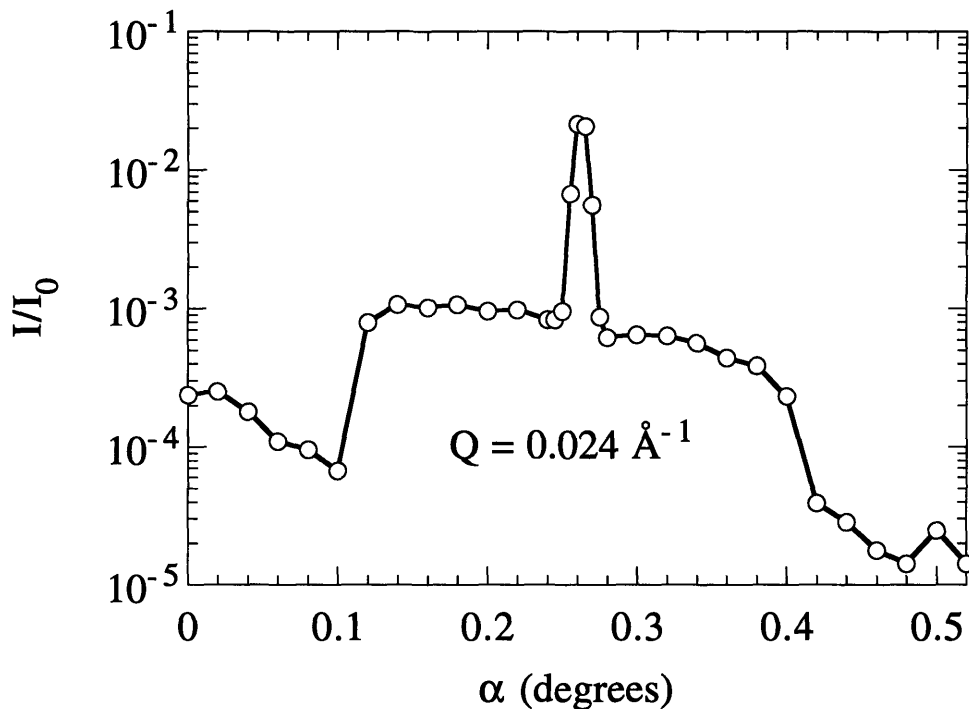
Figure 5-3: Rocking curve at $Q = 0.024\,\text{Å}^{-1}$.

theoretical reflectivity curve using the recursion relation in Equation 2.33. Fitting the measured reflectivity data results in the scattering length density profile shown in the inset of Figure 5-4. This profile generates the reflectivity curve shown as the solid line in the main figure and corresponds to a surface domain size $d_s = 270 \pm 2\,\text{Å}$ and correlation length $\xi_s = 217 \pm 6\,\text{Å}$. The slight discrepancies between the experimental data and the theoretical fit at $Q \approx 0.05\,\text{Å}^{-1}$ are due to higher-order Fourier modes in the scattering length density profile and do not significantly affect the determination of the surface domain size and correlation length.

Compared with the bulk parameters found from Figure 5-1, d_s is slightly smaller than d_b while ξ_s is significantly larger than its respective bulk value ξ_b. These results are surprising and demonstrate that the interfacial structure of a microemulsion cannot be quantitatively inferred from its bulk correlation function. Thus, we need to look beyond the simple Ginzburg-Landau Hamiltonian of Equation 5.1 in order to explain the surface structure of the microemulsion.
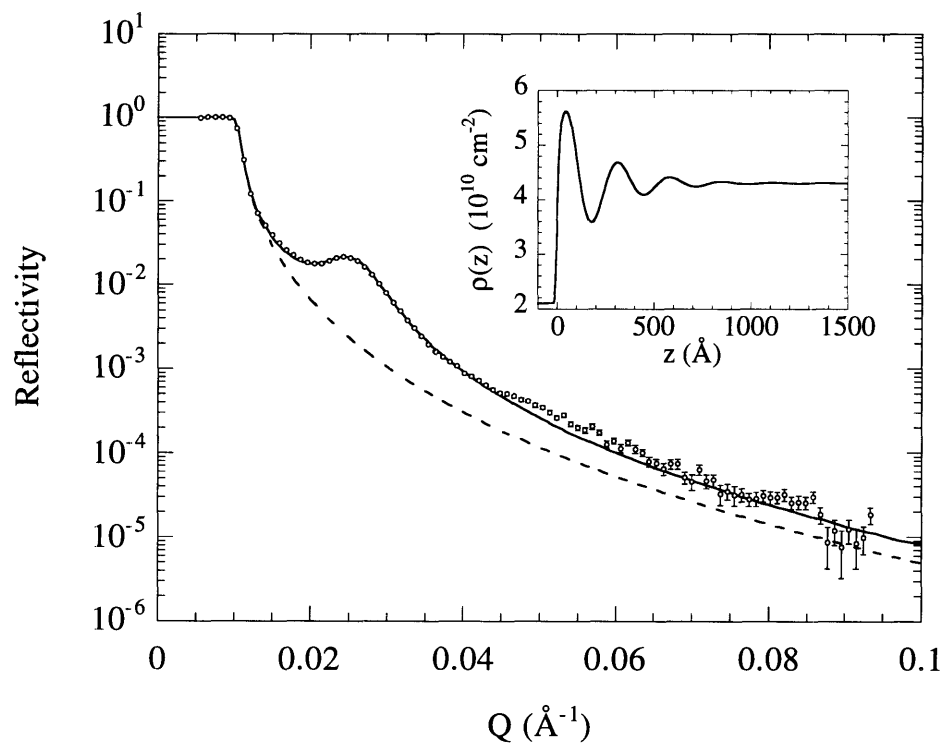
Figure 5-4: Specular reflectivity data with the fitted scattering length density profile in the inset.
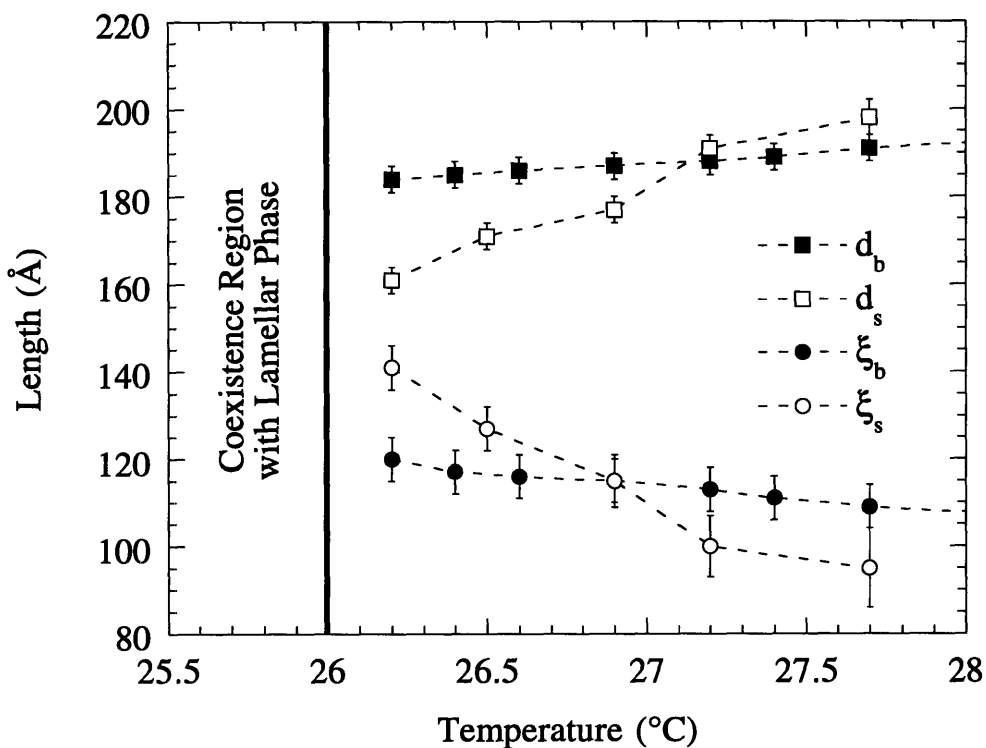
Figure 5-5: Variation of the bulk and surface length scales with temperature.

5.4 Curvature Effects

We next measured microemulsion samples composed of 20.0% surfactant, 40.0% water, and 40.0% oil with small angle neutron scattering and neutron reflectivity in the temperature range $26 < T < 28\,^{\circ}\mathrm{C}$. As discussed earlier in Figure 4-7, the surfactant monolayers in these microemulsions preferentially curve towards the water domains and the mean curvature of the surfactant film varies linearly with temperature in this range. To see the effect of curvature on the bulk and surface correlations of these microemulsions, the bulk domain sizes and correlation lengths and the surface domain sizes and correlation lengths were determined from the scattering and reflectivity data. Figure 5-5 shows the corresponding changes in the bulk and surface length scales as a function of temperature. The bulk and surface lengths show the same general trends as the temperature is decreased and the first-order lamellar transition is approached: both domain sizes decrease while the correlation lengths

71

increase. However, it is apparent that the curvature of the monolayers modifies the surface structure of the microemulsion to a far greater extent than it affects the bulk correlations.

There are several possible reasons as to why the fluctuations of the surfactant monolayers near the silicon surface are quantitatively different than their behavior in the bulk phase. Long-range van der Waals forces between the solid and the microemulsion may modulate the decay of surface correlations. But such interactions are relatively insensitive to temperature changes whereas the surface domain sizes and correlation lengths vary greatly with temperature in Figure 5-5. Another possibility is that the harmonic Hamiltonian does not adequately describe the physics of the surfactant monolayers in the microemulsion. Equation (5.1) was derived assuming only small deviations in $\psi(\vec{r})$ and its derivatives whereas the surfactant monolayers in the microemulsion strongly segregate distinct water and oil domains. Thus, as evidenced by the fluctuation-induced description of the first-order lamellar phase transitions, higher-order terms must be taken into account [73].

Anharmonic terms become especially important when the curvature of the surfactant monolayer breaks the symmetry between the water and oil in the microemulsion. The Hamiltonian in Eq. (5.1) only contains square terms that display $\psi \mapsto -\psi$ symmetry. In order to describe spontaneous curvature in the monolayer, additional terms of odd order will be needed. Because the overall volume fractions of water and oil in these microemulsions are the same, the Ginzburg-Landau expansion should continue to exhibit a minimum at $\psi = 0$ which precludes the term linear in ψ. The Laplacian term $\nabla^2 \psi$ is completely integrable and is actually equivalent to the surface field associated with s_1' in Equation 5.5. Thus, the lowest order terms that need to be considered are cubic ones:

$$\mathcal{H}_c = \int \left[c\,\psi^3 + c'\psi^2(\vec{\nabla}^2\psi) \right] d^3\vec{r}. \tag{5.8}$$

The effects of the cubic terms in Equation 5.8 can be treated perturbatively. In the calculation of the bulk correlation function and of $\langle \psi(\vec{q})\,\psi(-\vec{q}) \rangle$, the leading
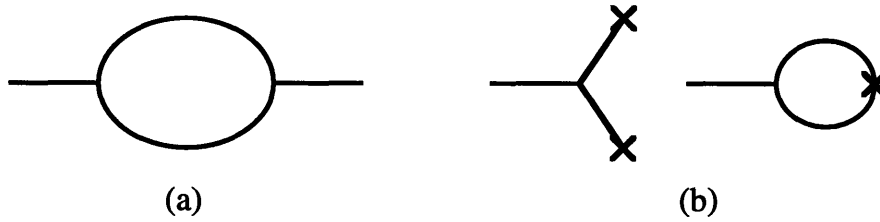
Figure 5-6: Diagrammatic representations of the curvature corrections to the (a) bulk and (b) surface correlations.

perturbative diagrams are of the form shown in Figure 5-6(a) [74]. The corrections are quadratic in c and c', and for small curvatures they will have only a slight effect on the bulk correlation function. On the other hand, terms due to spontaneous curvature can enter the surface profile calculation for $\langle \psi(q_z) \rangle$ to linear order as illustrated in Figure 5-6(b). The cubic terms in Equation (5.8) couple with surface field terms represented by lines attached with "×" markers to yield corrections on the order of cs_1^2, $c's_2$, etc. These diagrams explain the significant influence curvature has on renormalizing the surface domain size and correlation length in the microemulsion while at the same time only weakly perturbing the parameters of the bulk correlation function.

To make this analysis of the curvature corrections more quantitative and complete, additional measurements of the bulk and surface structure of microemulsions will have to be made. A wider range of temperature would be useful in determining how large of an effect curvature has on the surface and bulk correlations. Systematically varying the surface potentials using different silicon surface treatments and studying the resulting changes in the interfacial structure of the microemulsion would also be very valuable.

Nevertheless, we have seen that although the simple Ginzburg-Landau Hamiltonian can qualitatively describe the bulk and surface correlations in a microemulsion, the fluctuations of the surfactant monolayers near a solid surface are quantitatively different than those in the bulk microemulsion. By breaking the symmetry between

the water and oil domains in the microemulsion, curvature plays an important role in determining the interfacial properties of the surfactant monolayers in the microemulsion.

Chapter 6

Conclusions

We have seen that the surfactant monolayers in microemulsions exhibit an exceedingly rich phase behavior and represent a very complex statistical mechanical system. Here we studied some of the intrinsic characteristics of a single surfactant monolayer that was prepared at an oil-water interface in equilibrium with a middle-phase microemulsion. Using x-ray reflectivity, we obtained a scattering spectrum from the monolayer that was described in terms of a capillary wave model. We discovered that the interfacial tension and effective bending rigidity is very small, indicating that the statistical fluctuations of the oil-water interface are due to the interfacial properties of a saturated surfactant monolayer.

We also deduced the geometry of the surfactant monolayers residing within a bicontinuous microemulsion by determining the various interfacial areas of the surfactant film. Using contrast variation and small angle neutron scattering, we measured the different interfacial areas and calculated the curvature of the monolayers in the microemulsion. We found that at the temperature where the hydrophilicity and hydrophobicity of the surfactant is balanced, the monolayer has nearly zero mean curvature. When the temperature is varied, the surfactant monolayers curves preferentially towards either the water or oil phase.

We could characterize the size of the water and oil domains and the disorder of the monolayers inside a microemulsion using a Ginzburg-Landau theory. A simple harmonic Hamiltonian predicted that the structure of the surfactant monolayers near

a surface should be related to the bulk correlation function. When we measured the surface structure of the microemulsion using neutron reflectivity, we found the surface correlation lengths to be significantly different from the bulk correlation lengths. Accounting for spontaneous curvature in the surfactant monolayer, we attributed this effect to higher order terms in the Ginzburg-Landau theory.

Thus, we have seen that the properties of surfactant monolayers in solution with water and oil can generally be understood in terms of simple physical principles. However, until recently, we had very little quantitative information about their microscopic behavior in microemulsions. We show here that x-ray and neutron scattering techniques can be used to provide detailed knowledge about the statistical fluctuations and interfacial properties of surfactant monolayers in microemulsion systems. We believe that continuing work with scattering and similar techniques will provide even greater insight into the behavior of these complex fluids.

Bibliography

[1] R. J. Seeger, *Benjamin Franklin, New World Physicist* (Pergamon, Oxford, 1973).

[2] C. V. Boys, *Soap Bubbles, their Colours and the Forces which Mould them* (Dover, New York, 1959).

[3] C. Isenberg, *The Science of Soap Films and Soap Bubbles* (Tieto, Clevedon, 1978).

[4] *Physics of Amphiphilic Layers*, edited by J. Meunier, D. Langevin, and N. Bocarra (Springer, Berlin, 1987).

[5] *Statistical Mechanics of Membranes and Surfaces*, edited by D. Nelson, T. Piran, and S. Weinberg (World Scientific, Singapore, 1989).

[6] *Structure and Dynamics of Strongly Interacting Colloids and Supramolecular Aggregates in Solution*, edited by S. H. Chen, J. S. Huang, and P. Tartaglia (Kluwer, Dordrecht, 1992).

[7] *The Structure and Conformation of Amphiphilic Membranes*, edited by R. Lipowsky, D. Richter, and K. Kremer (Springer, Berlin, 1992).

[8] *Micelles, Membranes, Microemulsions, and Monolayers*, edited by W. M. Gelbart, A. Ben-Shaul, and D. Roux (Springer-Verlag, New York, 1994).

[9] G. Porte, J. Marignan, P. Bassereau, and R. May, J. Physique **49**, 511 (1988).

[10] J. Charvolin, Contemp. Phys. **31**, 1 (1990).

[11] M. Kahlweit, R. Strey, R. Schomäcker, and D. Hasse, Langmuir **5**, 305 (1989).

[12] M. Kahlweit, R. Strey, P. Firman, D. Haase, J. Jen, and R. Schomäcker, Langmuir **4**, 499 (1988).

[13] M. Kahlweit *et al.*, J. Colloid Interface Sci. **118**, 436 (1987).

[14] D. D. Lee, J. H. Choy, and J. K. Lee, J. Phase Equil. **13**, 365 (1991).

[15] R. Strey, Ber. Bunsenges. Phys. Chem. **97**, 742 (1993).

[16] W. D. Bancroft, J. Phys. Chem. **17**, 501 (1913).

[17] W. Jahn and R. Strey, J. Phys. Chem. **92**, 2294 (1988).

[18] N. F. Berk, Phys. Rev. Lett. **58**, 2718 (1987).

[19] N. F. Berk, Phys. Rev. A **44**, 5069 (1991).

[20] S. H. Chen, S. L. Chang, and R. Strey, J. Appl. Crystallogr. **24**, 721 (1991).

[21] S. H. Chen, D. D. Lee, and S. L. Chang, J. Mol. Struct. **296**, 259 (1993).

[22] M. Teubner, Europhys. Lett. **14**, 403 (1991).

[23] L. E. Scriven, Nature **263**, 123 (1976).

[24] J.-F. Bodet, J. R. Bellare, H. T. Davis, L. E. Scriven, and W. G. Miller, J. Phys. Chem. **92**, 1898 (1988).

[25] B. Widom, J. Chem. Phys. **84**, 6943 (1986).

[26] K. A. Dawson, Phys. Rev. A **35**, 1766 (1987).

[27] G. Gompper and M. Schick, in *Micelles, Membranes, Microemulsions, and Monolayers*, edited by W. M. Gelbart, A. Ben-Shaul, and D. Roux (Springer-Verlag, New York, 1994).

[28] P. G. de Gennes and C. Taupin, J. Phys. Chem. **86**, 2294 (1982).

[29] J. Jouffroy, P. Levinson, and P. G. de Gennes, J. Phys. (Paris) **43**, 1241 (1982).

[30] S. A. Safran, D. Roux, M. E. Cates, and D. Andelman, Phys. Rev. Lett. **57**, 491 (1986).

[31] M. Spivak, *A Comprehensive Introduction to Differential Geometry* (Publish or Perish, Berkeley, 1979).

[32] W. Helfrich, Z. Naturforsch. **A 33**, 305 (1978).

[33] P. Pieruschka and S. A. Safran, Europhys. Lett. **22**, 625 (1993).

[34] *Neutron, X-Ray and Light Scattering: Introduction to an Investigative Tool for Colloidal and Polymeric Systems*, edited by P. Lindner and T. Zemb (Elsevier, Amsterdam, 1991).

[35] R. L. Liboff, *Introductory Quantum Mechanics* (Addison-Wesley, Reading, MA, 1992).

[36] L. A. Feigin and D. I. Svergun, *Structure Analysis by Small-Angle X-Ray and Neutron Scattering* (Plenum Press, New York, 1987).

[37] D. D. Lee, J. Barker, and S. H. Chen, J. Phys. (Paris) IV **C8**, 431 (1993).

[38] P. Debye and A. M. Bueche, J. Appl. Phys. **20**, 518 (1949).

[39] G. Porod, in *Small-Angle X-ray Scattering*, edited by O. Glatter and O. Kratky (Academic, New York, 1982).

[40] L. G. Parratt, Phys. Rev. **95**, 359 (1954).

[41] S. K. Sinha, E. B. Sirota, S. Garoff, and H. B. Stanley, Phys. Rev. B **38**, 2297 (1988).

[42] R. Pynn, Phys. Rev. B **45**, 602 (1992).

[43] B. R. McClain, D. D. Lee, B. L. Carvalho, S. G. J. Mochrie, S. H. Chen, and J. D. Litster, Phys. Rev. Lett. **72**, 246 (1994).

[44] A. Braslau, M. Deutsch, P. S. Pershan, A. Weiss, J. Als-Nielsen, and J. Bohr, Phys. Rev. Lett. **54**, 114 (1985).

[45] A. Braslau, P. S. Pershan, G. Swislow, B. M. Ocko, and J. Als-Nielsen, Phys. Rev. A **38**, 2457 (1988).

[46] D. K. Schwartz, M. L. Schlossman, E. H. Kawamoto, G. J. Kellogg, P. S. Pershan, and B. M. Ocko, Phys. Rev. A **41**, 5687 (1990).

[47] M. K. Sanyal, S. K. Sinha, K. G. Huang, and B. M. Ocko, Phys. Rev. Lett. **66**, 628 (1991).

[48] B. M. Ocko, Phys. Rev. Lett. **64**, 2160 (1990).

[49] B. R. McClain, Ph.D. thesis, Massachusetts Institute of Technology, 1993.

[50] L. Nevot and P. Croce, Rev. Phys. Appl. **15**, 761 (1980).

[51] *Fluid Mechanics*, edited by L. D. Landau and E. M. Lifshitz (Pergamon, Oxford, 1986).

[52] Y. Yoneda, Phys. Rev. **131**, 2010 (1963).

[53] L. T. Lee, D. Langevin, J. Meunier, K. Wong, and B. Cabane, Prog. Colloid Polym. Sci. **81**, 209 (1990).

[54] D. D. Lee and S. H. Chen, Phys. Rev. Lett. **73**, 106 (1994).

[55] S. A. Safran, *Statistical Thermodynamics of Thermodynamics of Surfaces, Interfaces, and Membranes* (Addison-Wesley, Reading, MA, 1994).

[56] L. Auvray, J.-P. Cotton, R. Ober, and C. Taupin, J. Phys. (Paris) **45**, 913 (1984).

[57] L. Auvray, J.-P. Cotton, R. Ober, and C. Taupin, J. Phys. Chem. **88**, 4586 (1984).

[58] H. B. Stuhrmann, J. Appl. Crystallogr. **7**, 173 (1974).

[59] M. Teubner, J. Chem. Phys. **92**, 4501 (1990).

[60] M. Teubner, J. Chem. Phys. **95**, 5072 (1991).

[61] V. F. Sears, Neutron News **3**, 26 (1992).

[62] M. Kahlweit, R. Strey, and G. Busse, Phys. Rev. E **47**, 4197 (1993).

[63] R. Strey, J. Winkler, and L. Magid, J. Phys. Chem. **95**, 7502 (1991).

[64] J. S. Pedersen, D. Posselt, and K. Mortensen, J. Appl. Crystallogr. **23**, 321 (1990).

[65] J. Schelten and W. Schmatz, J. Appl. Crystallogr. **13**, 385 (1980).

[66] R. Strey, Colloid Polym. Sci. **272**, 1005 (1994).

[67] R. Kirste and G. Porod, Kolloid Z. Z. Polym. **184**, 1 (1962).

[68] G. Gompper and M. Schick, Phys. Rev. Lett. **62**, 1647 (1989).

[69] G. Gompper and M. Schick, Phys. Rev. Lett. **65**, 1116 (1990).

[70] G. Gompper and M. Schick, in *Phase Transitions and Critical Phenomena*, edited by C. Domb and J. Lebowitz (Academic, London, 1994), Vol. 16.

[71] M. Teubner and R. Strey, J. Chem. Phys. **87**, 3195 (1987).

[72] X. L. Zhou, L. T. Lee, S. H. Chen, and R. Strey, Phys. Rev. A **46**, 6479 (1992).

[73] S. A. Brazovskii, Zh. Eksp. Teor. Fiz. **68**, 175 (1975), [Sov. Phys. JETP **41**, 85 (1975)].

[74] D. J. Amit, *Field theory, the renormalization group, and critical phenomena* (McGraw-Hill, New York, 1978).